Where are the proto-South China Sea slabs? SE Asian plate tectonics and mantle flow history from global mantle convection modeling

Author names

Yi-An Lin[1], Lorenzo Colli,[1] Jonny Wu[1]

Affiliations

[1]Department of Earth and Atmospheric Sciences, University of Houston

Corresponding author: Yi-An Lin (ylin51@uh.edu)

Key Points:

- Four fully-kinematic, end-member SE Asian plate tectonic models were input into global geodynamic models
- Geodynamic models compared to tomography by converting temperature fields to seismic velocities and using P- and S-wave tomographic filters
- Double-sided proto-South China Sea subduction and early Borneo rotation during Eocene produces the mantle structure that best fits tomography

Abstract

The plate tectonic history of the hypothesized 'proto-South China Sea' (PSCS) ocean basin and surrounding SE Asia since Cenozoic times is controversial. We implement four diverse proto-South China Sea plate reconstructions into global geodynamic models to constrain PSCS plate tectonics and possible slab locations. We consider: southward versus double-sided PSCS subduction models; earlier (Eocene) or later (late Oligocene) initiation of Borneo counterclockwise rotations; and, larger or smaller reconstructed Philippine Sea plate sizes. We compare our modeling results against tomographic images by taking into account mineralogical effects and the finite resolution of seismic tomography. All geodynamic models reproduce the tomographically-imaged Sunda slabs beneath Peninsular Malaysia, Sumatra and Java. Southward PSCS subduction produces slabs beneath present Palawan, northern Borneo, and offshore Palawan. Double-sided PSCS subduction combined with earlier Borneo rotations uniquely reproduces sub-horizontal slabs under the southern South China Sea (SCS) at ~400 to 700 km depths; these models best fit seismic tomography. A smaller Philippine Sea (PS) plate with a ~1000 km-long restored Ryukyu slab was superior to a very large PS plate. Taken together, the four end-member plate models predict PSCS slabs at <900 km depths under present-day Borneo, the SCS, the Sulu and Celebes seas, and the southern Philippines. Regardless of plate models, we predicted passive mantle upwellings under Indochina during late Eocene-Oligocene times, and downwellings under the SCS during the late Cenozoic that do not support a deep-origin 'Hainan plume'. Modeled Sundaland dynamic topography depends strongly on the imposed plate model, varying by several hundred meters.

Plain Language Summary

The past motion of tectonic plates (i.e. plate tectonic reconstructions) is the source of fundamental boundary conditions for many studies of Earth history. The South China Sea lies at a key junction between northeast and southeast Asia, which is one of the most tectonically complex regions in the world. A great diversity of plate reconstructions have been proposed for the South China Sea area. Each reconstruction predicts that different amounts of cold lithospheric material have been subducted into the Earth's mantle at different times and in different places; therefore, implies a different Earth's mantle structure at present day. In this work we study the implications of each reconstruction by assimilating it into a numerical model of mantle convection, in the form of a time-dependent velocity boundary condition at the Earth's surface. This technique leads to a prediction for the time evolution of mantle structure and its flow field that is consistent with the reconstructed plate motions. We compare each predicted present-day mantle structure against seismic tomographic images of the Earth's mantle, testing the underlying reconstructions and their implications for southeast Asian plate tectonics. For each plate reconstruction we also computed the warping of the Earth's surface caused by the mantle flow.

1. Introduction

Southeast Asia is located between the major Indo-Australian, Eurasian, and Pacific plates, within one of the most tectonically-complex regions on Earth (Fig. 1a). Published Southeast Asian plate tectonic reconstructions generally show the region has been dominated by marginal sea opening, subduction, collision and terrane accretion during Cenozoic times, but many details are debated (e.g. Hall, 2012; Wu & Suppe, 2018). The aim of this paper is to investigate the Cenozoic plate tectonic and mantle flow histories of the South China Sea (SCS) region, and in particular, the enigmatic 'proto-South China Sea' (PSCS) ocean basin (Fig. 1b) (Cullen, 2010; Hall, 2012; Holloway, 1982; Taylor & Hayes, 1983; Wu & Suppe, 2018). The PSCS is a hypothesized ocean basin (Fig. 1b) that possibly existed in the early Cenozoic near the present SCS and was consumed during SCS opening (Holloway, 1982). The vanished PSCS was primarily proposed to account for a spatial gap in Southeast Asia plate reconstructions prior to the mid-Cenozoic, before the main period of SCS spreading (Fig. 1b). However, the former location, size, lithospheric nature, and eventual demise of the PSCS has been highly debated (Figs. 2d) (Cullen, 2014; Hall, 2012; Rangin et al., 1999; Wu & Suppe, 2018). Alternatively, another class of models have argued that a PSCS ocean basin never existed; instead, these models invoke Southeast Asia 'extrusion' (Fig. 2c), which is the southeastward translation of lithospheric blocks due to the India-Asia collision (Tapponnier et al., 1982), to account for the plate reconstruction gap in Figure 1b. Recent studies have recognized the importance of including mantle tomographic model constraints within Southeast Asian plate tectonic models (Hall & Spakman, 2015; Tang & Zheng, 2013; Wu & Suppe, 2018; Wu et al., 2016). However, there is no agreement on the

89 present location of the PSCS slabs (Fig. 2d). As a result, PSCS plate tectonic models that include

90 mantle constraints (i.e. slabs) also show strongly contrasted histories (Figs. 2a, b).

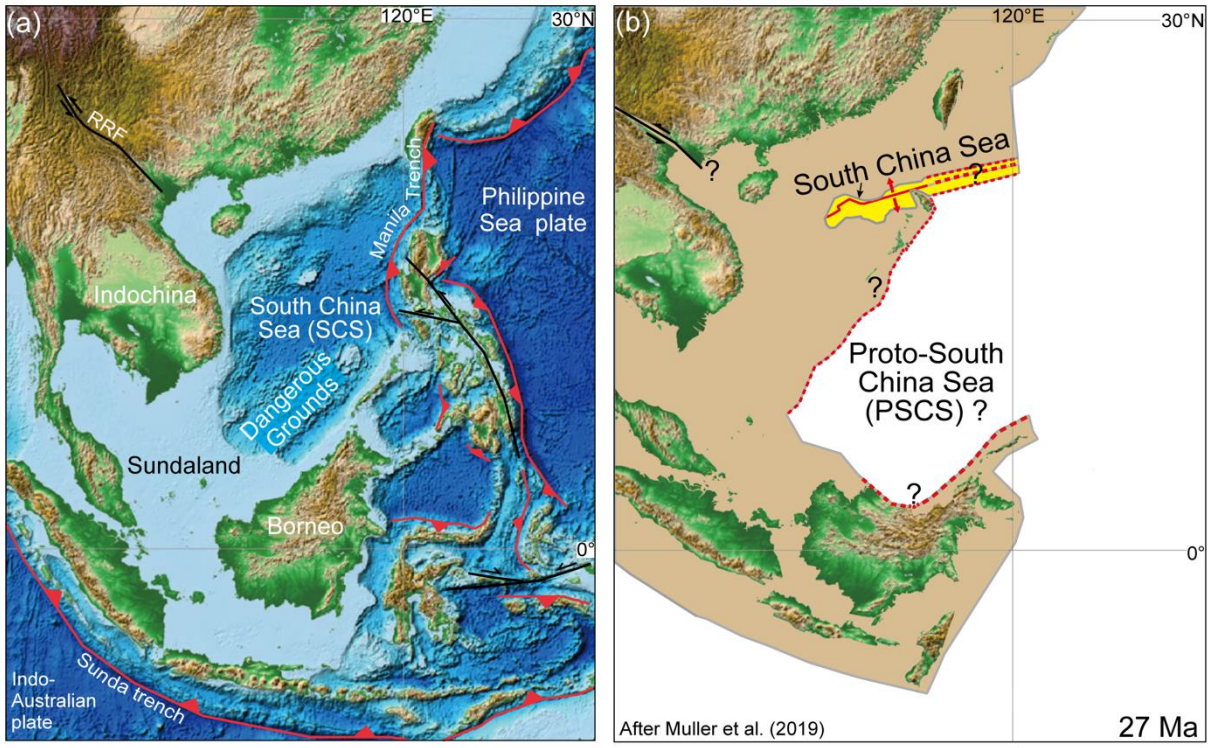

91

92 **Figure 1.** (a) Present-day tectonic setting of the South China Sea (SCS) and surrounding
93 southeast Asia after Hall (2012) and Cullen et al. (2012). Red lines indicate subduction zones
94 and triangle teeth point to the overriding plate. Black lines indicate major strike slip faults, (b)
95 Plate reconstruction of SCS area during the Oligocene, prior to the main phase of SCS spreading
96 (after Müller et al., 2019). The hypothesized proto-South China Sea (PSCS) ocean basin is
97 thought to have existed within the plate reconstruction gap (white areas) between the SCS and
98 Borneo. RRF: Red River fault.
99

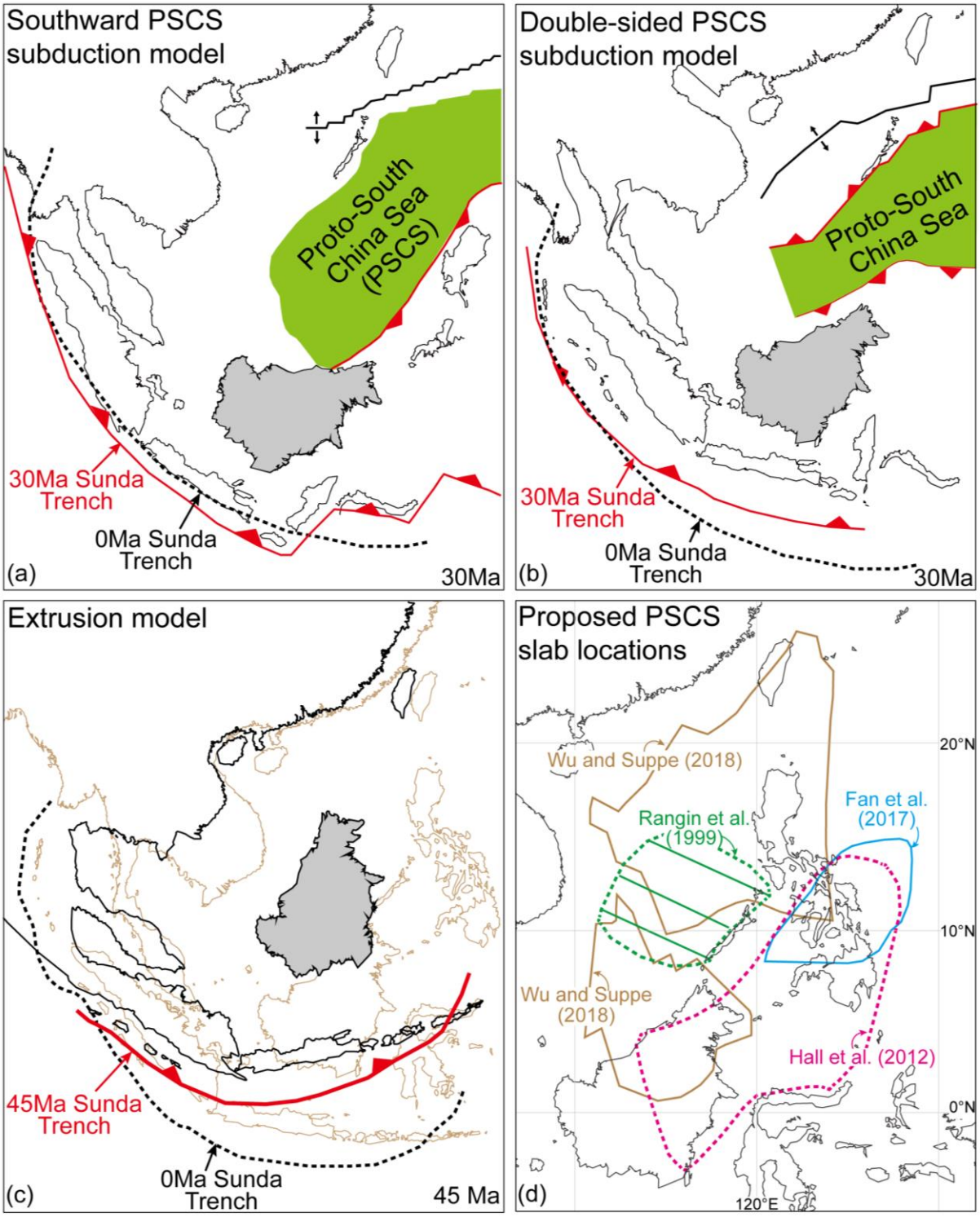

Figure 2. Proposed plate tectonic reconstructions of SE Asia during early to mid-Cenozoic times showing differences in the reconstructed proto-South China Sea subduction boundaries and paleo-Sunda trench locations: (a) the southward PSCS subduction model (after Hall, 1996; Holloway, 1982; Taylor & Hayes, 1983).; (b) double-sided subduction model (Wu and Suppe,

2018); (c) Extrusion model (after Replumaz & Tapponnier, 2003). (d) Map showing various PSCS slab locations proposed by previous studies. There is little agreement on the present whereabouts of the PSCS subducted lithosphere, if such exist. The shown PSCS slab locations vary between 500 to 800 km depths in the mantle.

Previous studies indicate that a clearer understanding of PSCS plate tectonics may explain the enigmatic initiation and rift evolution of the present SCS, which has been the subject of recent ocean drilling and geophysical studies but continues to puzzle (Jian et al., 2019; Sun et al., 2019; Wang et al., 2019). PSCS histories also potentially provide a means for linking Southeast Asia to the South China Eurasian continental margin prior to mid-Cenozoic times (Wu & Suppe, 2018), which is important for global plate tectonic models. Sundaland basin formation, uplift, and SCS post-rift magmatism in the Cenozoic continue to challenge our current understanding of plate tectonics, and recently, deep mantle processes have been proposed to explain these phenomena (Roberts et al., 2018; Yang et al., 2016; Zahirovic et al., 2016). Previous geodynamic studies attempt to address these have relied on assimilation of a single input plate tectonic model; in other words, only one class of PSCS plate models has been considered in Southeast Asia geodynamic models (Fig. 2a) (Yang et al., 2016; Zahirovic et al., 2016).

In this paper, we show the first suite of Southeast Asia geodynamic models that incorporate alternative, end-member PSCS plate model histories to test previous results and discuss a fuller range of outcomes. We aim to constrain the possible present locations of the PSCS slabs (if such exist) within the present Southeast Asian mantle by examining four forward global geodynamic models that implement the diverse, end-member PSCS and surrounding Southeast Asia plate tectonic reconstructions. We compared our geodynamic models to imaged mantle structure

129 from seismic tomography by converting model temperature fields to seismic velocities and
130 applying P- and S-wave tomographic filters. We analyze a range of possible Southeast Asian
131 mantle flow histories and discuss these histories against the viability of a deep-origin 'Hainan
132 plume' mantle upwelling, Sundaland basin formation in the Oligocene, and Southeast Asia
133 dynamic topography (i.e. uplift or subsidence due to viscous stresses from mantle convection).
134
135 *1.1 Review of South China Sea region plate tectonic reconstructions*
136
137 A great diversity of plate tectonic reconstructions has been proposed for the SCS and
138 surrounding Southeast Asia regions since the Cenozoic (e.g. Figs 2, 3) and are tested here
139 through geodynamic modeling. A major challenge for Southeast Asia plate models is to
140 reconstruct a region that is a loose collection of terrane fragments, blocks and transient
141 marginal seas that are not well-constrained by traditional seafloor spreading-based plate
142 tectonics (i.e. global plate models). As a result, multiple explanations have arisen to account for
143 the formation of the relatively large (>700 km N-S extent) SCS ocean basin in the mid-Cenozoic.
144 The most popular models account for SCS opening by southeastward subduction of the PSCS
145 beneath NW Borneo during Eocene to Miocene times (Fig. 2a) (Hall, 1996; Holloway, 1982;
146 Taylor & Hayes, 1983). We herein call this the 'southward subduction model' (Fig. 2a). In this
147 model, slab pull from PSCS southward subduction drives SCS opening (Hall, 1996; Holloway,
148 1982; Taylor & Hayes, 1983). Southward subduction models differ on the amount of subducted
149 PSCS, with some models preferring a 'hybrid' solution that includes southward subduction of a
150 relatively smaller PSCS, and limited Southeast Asia extrusion (Cullen, 2010). The southward

subduction model was primarily developed from regional geology, seafloor spreading, and magmatism (Holloway, 1982; Hutchison, 2004; Taylor & Hayes, 1983), and is thus most consistent with these constraints. However, the southward subduction model has not been easily linked to mantle structure. Various slab-like, fast tomographic anomalies within the Southeast Asian mantle (i.e. to the north, east and southwest of the present SCS) have been attributed to southward PSCS subduction (see review in 1.2), with little agreement between studies (Fig. 2d) (Fan et al., 2017; Hall & Spakman, 2015; Rangin et al., 1999). In this study, we assimilate two variants of southward subduction models into geodynamic models (Table 1) to model possible PSCS slab locations under Southeast Asia, given this plate tectonic history.

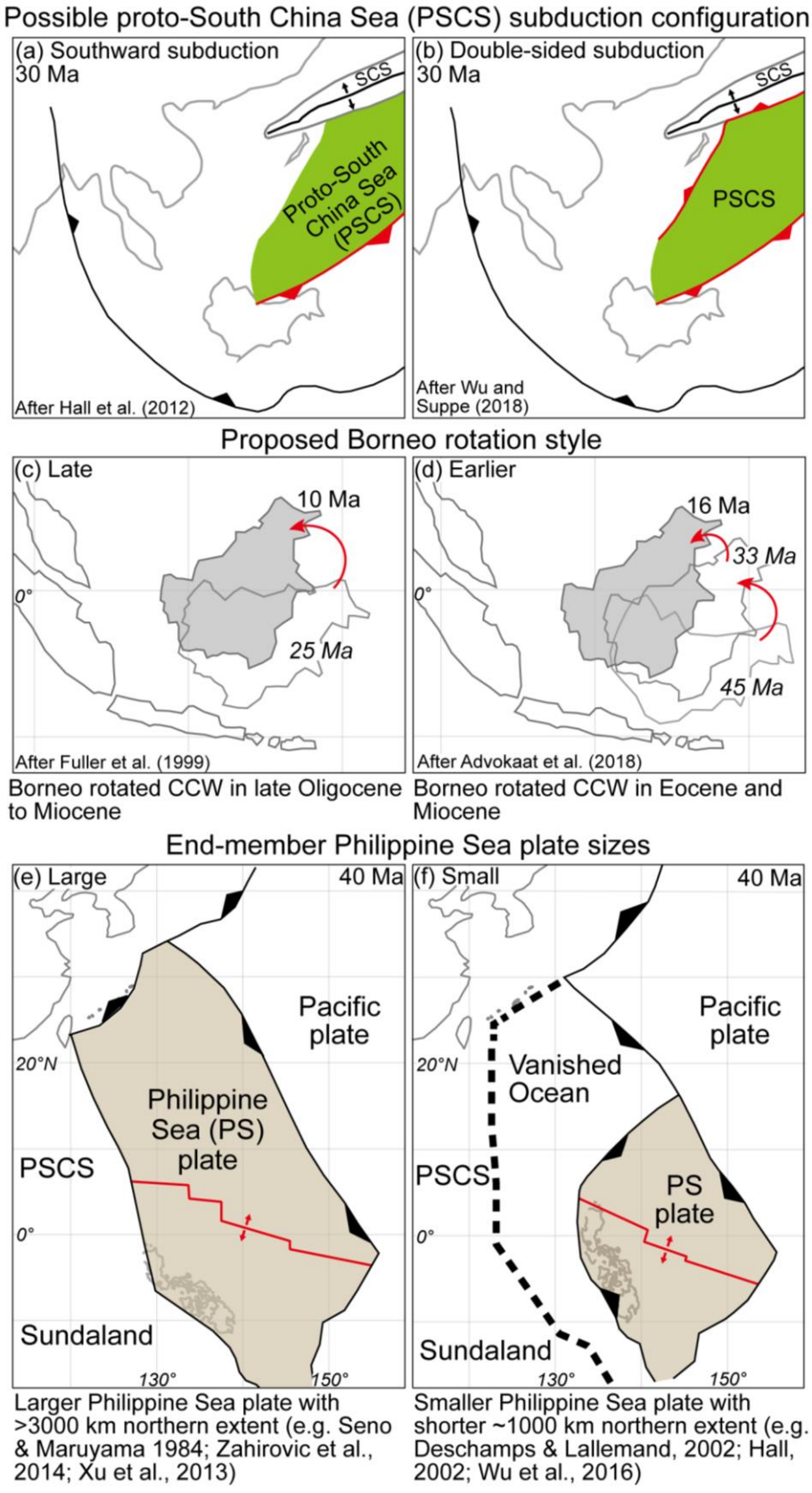
Possible proto-South China Sea (PSCS) subduction configuration
(a) Southward subduction
30 Ma
SCS
Proto-South China Sea (PSCS)
After Hall et al. (2012)
(b) Double-sided subduction
30 Ma
SCS
PSCS
After Wu and Suppe (2018)
Proposed Borneo rotation style
(c) Late
10 Ma
0°
25 Ma
After Fuller et al. (1999)
(d) Earlier
16 Ma
33 Ma
0°
45 Ma
After Advokaat et al. (2018)
Borneo rotated CCW in late Oligocene to Miocene
Borneo rotated CCW in Eocene and Miocene
End-member Philippine Sea plate sizes
(e) Large
40 Ma
Pacific plate
20°N
Philippine Sea (PS) plate
PSCS
0°
Sundaland
130°
150°
(f) Small
40 Ma
Pacific plate
20°N
Vanished Ocean
PSCS
PS plate
0°
Sundaland
130°
150°
Larger Philippine Sea plate with >3000 km northern extent (e.g. Seno & Maruyama 1984; Zahirovic et al., 2014; Xu et al., 2013)
Smaller Philippine Sea plate with shorter ~1000 km northern extent (e.g. Deschamps & Lallemand, 2002; Hall, 2002; Wu et al., 2016)

Figure 3. Southeast Asian plate tectonic reconstruction parameters implemented into the geodynamic models in this study. (a) and (b) show the southward PSCS subduction and double-sided PSCS subduction models, respectively; (c) and (d) show later and earlier proposed Borneo counterclockwise rotations, respectively; and (e) and (f) show proposed larger and smaller end-member Philippine Sea (PS) plate sizes, respectively.

Wu and Suppe (2018) suggested an alternative "double-sided subduction model" (Fig. 2b) based on interpreted mantle structure that involved both northward and southward PSCS subduction during the mid-Cenozoic. In this model, the southern PSCS was initially subducted southward beneath Borneo as it rotated counter-clockwise at Early Eocene. Later, during 30 to 20 Ma the northern PSCS subducted northward under the opening SCS in a 'self-subduction' fashion similar to the western Mediterranean after the Oligocene time (Wu & Suppe, 2018). This plate model was based on tomographic profiles that showed two sets of PSCS slabs: a swath of shallower northern PSCS slabs under the present SCS, and deeper southern PSCS slabs under northern Borneo (Fig. 2d) (Wu & Suppe, 2018). Here we test whether the implementation of this plate model into a geodynamic model can reproduce the observed slabs, especially the northern PSCS slabs under the present SCS, which are the most controversial.

'Extrusion' models (Fig. 2c) suggest that the India-Asia collision caused the southeastward 'extrusion' of Southeast Asia, which led to SCS seafloor spreading and Borneo clockwise rotations in the Cenozoic (Tapponnier et al., 1982). Extrusion models imply that a PSCS plate never existed, and instead, SCS opening can be explained by southward expansion of Southeast Asia. Consequently, extrusion models imply two relatively testable predictions for Southeast Asian mantle structure: firstly, 'proto South China Sea' slabs do not exist within the Southeast Asian mantle; and secondly, the Sunda subduction zone south of Indonesia retreated

187 significantly during the Cenozoic (subduction zone indicated by bold red line in Fig. 2c) relative
188 to other models (e.g. Figs. 2a, b). In this study, we do not explicitly test the extrusion model
189 due to the complexities of building a suitable, topologically-closed full plate model but discuss
190 extrusion model viability based on our comparison between predicted and imaged mantle
191 structure under Southeast Asia.
192
193 *1.2 Previous Interpretations of proto-South China Sea slabs from tomography and their plate*
194 *tectonic implications*
195
196 Hall and Spakman (2015) interpreted detached PSCS slabs trending SW-NE at ~800 km depth
197 beneath central Borneo and the central Philippines from UUP07 P-wave global seismic
198 tomography model (Amaru, 2007) (Fig. 2d). It was suggested that the PSCS slabs lie further
199 south with respect to present Borneo because the PSCS subducted southward beneath NW
200 Borneo and the Cagayan ridge at 45-20 Ma, followed by counterclockwise rotation of Borneo
201 and the southeast margin of Sundaland between 30-10 Ma (Hall & Spakman, 2015). Fan et al.
202 (2017) interpreted detached PSCS slabs that were oriented NE-SW at 400-700 km depths
203 beneath the Luzon arc from their regional P-wave seismic tomography model (Fig. 2d). Their
204 identified PSCS slabs were deeper towards the southeast, which led to the interpretation that
205 PSCS closure started from the south and propagated toward the north due to collision between
206 the Palawan microcontinental block and the Philippine Mobile Belt, following previous studies
207 (Hall, 2002; Zahirovic et al., 2012). Rangin et al. (1999) interpreted detached PSCS slabs at ~500-
208 600 km depths beneath the present-day southeast SCS from seismic tomography model (Fig.

2d). It was suggested that the PSCS was a small ocean basin that subducted southwards beneath NW Borneo and the Cagayan ridge before the early Miocene (Rangin et al., 1999). The detached PSCS slabs are relatively far north with respect to present NW Borneo and Palawan due to clockwise rotation of Sundaland between 10 and 15 Ma (Rangin et al., 1999). Wu and Suppe (2018) mapped two sets of PSCS slabs from MITP08 P-wave seismic tomography model (Li et al., 2008) that included the detached PSCS north slabs (N-PSCS) at ~500-700 km depth under the present-day SCS and northern Luzon arc to eastern Taiwan, and detached PSCS south slabs (S-PSCS) at ~800 km depth beneath southern SCS and northern Borneo (Fig. 2d). The southernmost N-PSCS slabs interpreted by Wu and Suppe (2018) were also identified by Rangin et al. (1999) from other tomography. Wu and Suppe (2018) suggested that the S-PSCS slabs were subducted southward beneath Borneo as Borneo rotated counter-clockwise at Early Eocene; the N-PSCS slabs subducted northward beneath the southern SCS margin (i.e. Dangerous Grounds) during SCS opening ~30 to 15 Ma (Wu & Suppe, 2018). Tang and Zheng (2013) proposed a ~500 km fast anomaly dipping southeastward beneath north Borneo based on their regional S-wave velocity model for the upper mantle. As described above and shown in Figure 2, these PSCS slab interpretations are not equally compatible with all proposed plate tectonic reconstructions. In this paper, we construct four geodynamic models to explicitly predict the positions of subducted PSCS slabs (Table 1) and compare them against the various interpretations reviewed above.

2. Methods

2.1 Geodynamic Modeling

Geodynamic models have been used to test the mantle structure implications of an input plate model (e.g. Bunge & Grand, 2000; Nerlich et al., 2016; Zahirovic et al., 2016) but relatively few studies have been conducted for Southeast Asia due to the tectonic complexity of the region. Assimilation of a southward PSCS subduction plate model into a recent global geodynamic model provided many valuable insights for the region (Yang et al., 2016; Zahirovic et al., 2016) but did not reproduce the sub-horizontal slabs below the present SCS observed by Wu and Suppe (2018), thus partially motivating this study. Here we assimilate multiple end-member PSCS plate models into geodynamic models to further test the range of possibilities (Table 1; Fig. 3). Geodynamic models also imply the histories of mantle flow and dynamic topography, which is defined as warping of the Earth's surface due to viscous stresses within the mantle (Hager et al., 1985). Previous geodynamic models have predicted dynamic subsidence within Southeast Asia during the Cenozoic (Flament et al., 2013; Steinberger, 2007; Yang et al., 2016). and a deep-rooted 'Hainan plume' rising from the core mantle boundary (CMB) (Zhang & Li, 2018). We address these topics by analyzing and discussing mantle flow and dynamic subsidence histories in Southeast Asia from our geodynamic model outputs.

Table 1: List of the parameters used in each plate kinematic model

Model Name	PSCS subduction	Borneo CCW rotation	Philippine Sea plate size	Initial State
GPlates Default (model 0)	Southward	Later*	Large	460 Ma**
Southward Default (model 1a)	Southward	Later	Large	30 Ma
Double-sided Default (model 1b)	Double-Sided	Later	Large	30 Ma
Refined Southward (model 2a)	Southward	Earlier	Small	45 Ma
Refined Double-sided (model 2b)	Double-Sided	Earlier	Small	45 Ma

*Matthews et al. (2016) plate model has the inconsistency between Borneo rotation and the motion of the plate it sits on (section 2.1). Here referred to the rotation of Borneo island not the plate it sits on.
**Matthews et al. (2016) was assimilated from 460-0 Ma for GPlates default model. Other models used 30 Ma or 45 Ma mantle state as the initial state for the assimilation of the reconstructed plate models.

Table 1. List of the parameters used in each plate kinematic model. The GPlates default model was adapted from Matthews et al. (2016).

We modeled mantle convection by solving the equations of conservation of mass, momentum, and energy in the truncated anelastic liquid approximation for a compressible fluid with infinite Prandtl number in a spherical shell (Jarvis & McKenzie, 1980a) with the inner radius being the radius of the CMB (R_{CMB}), the outer radius being the radius of the Earth's surface (R_E). The equations have been solved numerically using the finite element code TERRA (Bunge et al., 1998). The computational domain is discretized on a regular grid based on the icosahedron, for a total of ~80 million grid points and a minimum resolution of ~25 km, allowing us to simulate convection in the same regime as the real Earth. The mantle is heated from below and from within. The viscosity is Newtonian and depends on temperature and depth as:

$$\eta(d,T) = \eta_0 A(d) \exp(V^* \frac{d}{R_E - R_{CMB}} - E^* \frac{T - T_S}{T_{CMB} - T_S})$$

where η_0 is the reference viscosity, A(d) is a radial prefactor to impose a low-viscosity asthenosphere, V^* and E^* are non-dimensional constants modulating the sensitivity of viscosity to temperature and depth variations, T_s is the surface temperature and T_{CMB} is the core mantle boundary temperature.

This rheology produces two-sided subduction and we do not force one-sided subduction by imposing either dipping weak plate boundaries or a prescribed dipping slab thermal structure. Slab material thus sinks vertically unless it is swept by mantle wind. The reference viscosity is set to 10^{22} Pas, giving a bottom heating Rayleigh number of $1.5*10^6$ and a mixed heating Rayleigh number of $7.6*10^7$ based on a volume-averaged viscosity. The CMB is modeled as a free-slip interface while a prescribed velocity field is imposed at the surface.

Table 2: Geodynamic model parameters employed in this study	
Rayleigh number	$7.63*10^7$
Reference viscosity	10^{22} Pa s
Volumetric mean mantle density	4448 kg/m^3
Thermal expansivity	$2.5*10^{-5}$ K^{-1}
Thermal conductivity	3.0 W m^{-1}K^{-1}
Surface temperature	300 K
CMB temperature	4200 K
Radiogenic heat production rate	$6*10^{-12}$ W kg^{-1}

Table 2. Parameters used in the geodynamic model.

2.2 Plate kinematic boundary conditions

278

279 In this study, we assimilate a suite of five contrasted PSCS and Southeast Asia plate models into
280 the geodynamic code TERRA (Fig. 4; Table 1). The implemented plate models were
281 reconstructed using the software GPlates as a set of continuously closing plates having a global
282 self-consistent velocity field (Gurnis et al., 2012). We extracted velocity vectors at each grid
283 point location at intervals of 1 Ma and imposed them as the surface velocity boundary
284 condition of the model. In this study the imposed surface velocities are the only difference
285 between different models and all geodynamic parameters are kept constant.

286

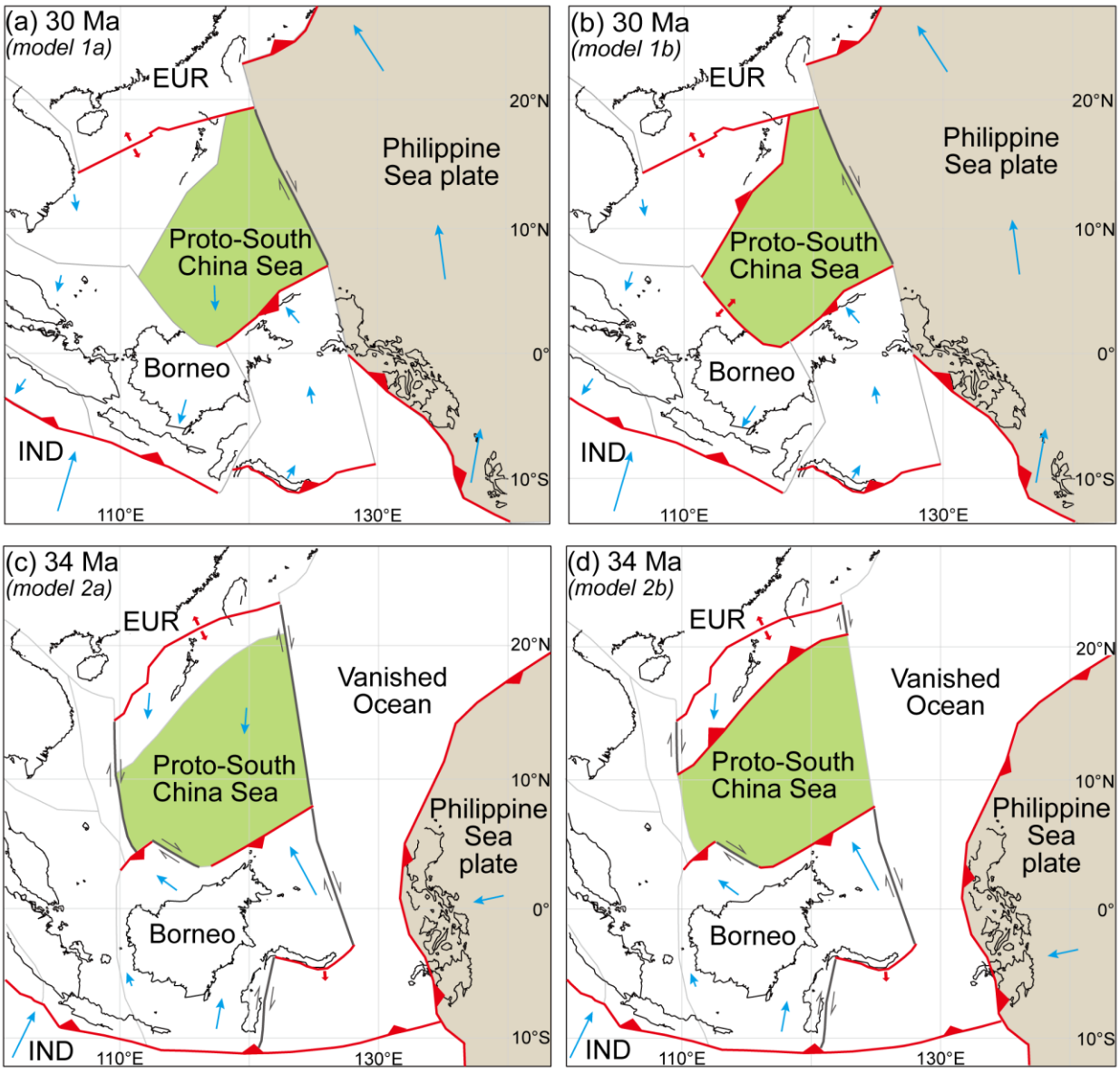

Figure 4. Representative maps showing the four main plate models that were assimilated into the geodynamic models in this study. (a) Reference Model 1a assimilated southwards PSCS subduction beneath NW Borneo, modified slightly from Matthews et al. (2016). (b) Reference Model 1b was identical to a) but implemented double-sided PSCS subduction following Wu and Suppe (2018). (c) and (d) show our 'refined' models 2a and 2b that implemented southward and double-sided subduction, respectively. The refined models 2a and 2b also included the following parameters: Borneo rotations following Advokaat et al. (2018) (see Fig. 3d), a smaller Philippine Sea plate (see Fig. 3f), and other minor modifications (see Sec. 2.1 for details). Blue arrows indicate the plate motion relative to Eurasia. Black lines show the coastline at 30 Ma (model 1a and 1b) and 34 Ma (model 2a and 2b). Grey lines show the plate boundaries.

The input plate models are broadly described below; further details are available in the Supplemental Text. We note our input plate models were optimized for investigating global tomography-scale (i.e. >100 km-scale) mantle structures. Thus, smaller-scale regional flaws and inevitable geological incompatibilities are present due to the limitations of rigid block models and challenges of integrating discrete published Sundaland plate models into a unified global solution. We will highlight and discuss the effects of these small plate model flaws where significant, but in general, we found most of the smaller regional flaws created negligible (i.e. below global tomography-scale) differences in final mantle structure.

'Default' Model 0 and 'Reference' models 1a, 1b

We implemented a global plate 'Model 0' from 460 to 0 Ma based on Matthews et al. (2016). We call Model 0 our 'default' model because it was assimilated for computational efficiency and not analyzed in detail (but was very similar to Model 1a). Instead, Model 0 was used to generate an 'initial state' for the other four main models in this study at 30 Ma or 45 Ma (Table 1). Specifically, the two reference models 1a and 1b based on Matthews et al. (2016) were assimilated from the 30 Ma mantle state of the default Model 0. Models 1a and 1b were designed to simulate end-member PSCS scenarios within the 'reference' context of Matthews et al. (2016). The reference Model 1a assimilated southwards PSCS subduction following Matthews et al. (2016); minimal modifications were added to improve self-consistency within Southeast Asia (see Supplemental Text). Our reference Model 1b was similar to Model 1a but

imposed an additional northward subduction zone at the northern PSCS margin to simulate double-sided PSCS subduction (compare Figs. 4a, b).

'Refined' models 2a and 2b

A second set of 'refined' models 2a and 2b were assimilated that added the following four refinements based on recent literature:

(1) the SCS was closed following the full-fit reconstruction stretching factor of Bai et al. (2015) to more realistically account for non-rigid plate behavior (i.e. continental stretching at the northern and southern SCS margins) (see Supplemental text). This had the effect of positioning the northern PSCS margin about 2°-3° closer to south China (i.e. further northwards) in the early Oligocene (Fig. 4).

(2) We followed the earlier Borneo rotation timings of Advokaat et al. (2018), in contrast to the later Borneo rotations of Fuller et al. (1999) that were already assimilated in our reference models 1a and 1b. Borneo ~50° counter-clockwise rotations during the Cenozoic have been interpreted from paleomagnetism (Advokaat et al., 2018; Fuller et al., 1999), but rotation timings are debated and have important effects on southward PSCS subduction. To maintain self-consistency within Sundaland, we also slightly adjusted the rotations of peninsular Malaysia, Java, and Sumatra and moved the NW Borneo subduction zone location slightly northward in Models 2a and 2b following Advokaat et al. (2018) (Fig. 4). Our integration of Advokaat et al. (2018) and Matthews et

al. (2016) within a rigid plate model produced an unwanted ‘edge effect’ narrow (~300 km) zone between Hainan Island and NE Borneo (see Model 2a, 2b plate animation movies) that is presently occupied by a number of elongate and complex sedimentary basins (Pubellier & Morley, 2014). No attempt was made to make this narrow plate model feature geologically-compatible; therefore, we will not analyze our results near NE Borneo area in detail.

(3) The Philippine Sea plate had important plate tectonic interactions with the SCS region after the mid-Cenozoic (Zhao et al., 2019). However, the pre-subduction Philippine Sea plate size is controversial due to subduction of the northern Philippine Sea plate under the Ryukyus (Figs. 3e, f). A ‘large’ plate has been proposed that includes a 3000 km-long reconstructed northern Philippine Sea slab (Fig. 3e) (Seno & Maruyama, 1984; Zahirovic et al., 2014). The large Philippine Sea was assimilated in the reference models 1a and 1b (Fig. 4a, b; Table 1) and has also been implemented in previous geodynamic models (Yang et al., 2016; Zahirovic et al., 2016). Here we implement an alternative ‘small’ Philippine Sea plate in our refined Models 2a and 2b (Figs. 4c, d; Table 1) based on published studies (Fig. 3f) (e.g. Hall, 2012; Pownall et al., 2017; Wu et al., 2016). To account for the space difference between the large and small Philippine Sea (Figs. 3e, f), we implemented a ‘vanished ocean’ plate that was stationary within Eurasian reference between the Philippine Sea, PSCS and Eurasia (Fig. 4c, d) following Wu et al. (2016). We acknowledge that other solutions within the area occupied by our modeled ‘vanished ocean’ are also possible (Hall, 2012; Ma et al., 2019). However, for brevity our later

discussion will mainly focus on the suitability of a larger or smaller reconstructed Philippine Sea and other details such as the possible vanished ocean will only be discussed briefly.

2.3 Mapping temperature to seismic velocity

The predicted present-day temperature fields were converted to seismic velocities using a thermodynamically self-consistent model of mantle mineralogy for a pyrolitic composition. Equilibrium mineral assemblages and elastic properties were computed using the software framework MMA-EoS (Chust et al., 2017) with thermoelastic data from Stixrude and Lithgow-Bertelloni (2011). We applied a correction for anelasticity effects after Karato (1993) using the radial Q profile of PREM, a frequency dependence $\alpha = 0.26$ and an activation enthalpy $H^* = 424$ KJ/mol. The seismic velocities thus obtained were then filtered using the resolution operators of the models LLNL-G3D-JPS (Simmons et al., 2015; Simmons et al., 2019) and S40RTS (Ritsema et al., 2011) to account for the finite and spatially variable resolution of these models. This ensures a more robust comparison of the predicted elastic structure against these two seismic tomography models. We also consider other P-wave seismic tomography models that are widely-used in our study area: MITP08 (Li et al., 2008), GAP_P4 (Fukao & Obayashi, 2013), and UUP07 (Amaru, 2007). As no explicit resolution operator is available for these models, they were compared against the full-resolution predicted elastic structures.

3. Results

Time-dependent cross sections of the thermal mantle heterogeneity field (Fig. 5, 6 and S3) can provide a detailed view of the slab sinking trajectories. In this section, we present the mantle thermal structure derived from each plate model.

Reference model 1a: southward proto-South China Sea subduction

The reference model 1a assimilated southward PSCS subduction that closely followed (Matthews et al., 2016) (see Methods; Supplemental Text). It was analyzed along A-A' transect across South China Sea (SCS) (Fig. 5). A 3D view of the mantle model along A-A' transect within the SCS is presented to allow visualization of both the mantle structure and progressive subduction of the proto-South China Sea (PSCS) (green region at the top surface in Fig. 5a). The model evolution from 30 to 0 Ma is presented in Figure 5a, whereas Figures 5b to f show a comparison of the velocity-converted and tomographically-filtered model results to actual global P- and S-wave seismic tomography model. The 30 Ma initial state shows the subducted Sunda (SUN) slabs (blue low-temperature anomalies) beneath the Java trench driven by convergence between the Indo-Australian and Eurasian plates (Fig. 5a). Slabs from Izanagi (IZA) subduction prior to the Eocene are visible below 500 km depth in the mantle beneath the Eurasian margin (Fig. 5a). SCS spreading displaces the cold lithosphere of Dangerous Grounds and produces young, warm asthenosphere upwellings under the SCS spreading ridge after 30 Ma (red, see Fig. 5a). At 24 Ma, the proto-South China Sea south (S-PSCS) slabs subducted southward beneath NW Borneo (Fig. 5a). At 18 Ma, very large Philippine Sea plate that was modeled to subduct beneath the Eurasian margin before 45 Ma (Matthews et al., 2016), named

paleo-Philippine Sea (P-PS) slab appeared within our cross-section due to minor lateral slab advections (Fig. 5a). By this period, the IZA slabs have sunk deeper than ~1000 km depths in the mantle beneath the Eurasian margin (Fig. 5a). From 30-15 Ma, the PSCS plate translated southward toward Borneo and Borneo rotated CCW; the PSCS plate began to subduct and formed the southward-subducted proto-South China Sea south (S-PSCS) slabs (Fig. 5a). From ~24-15 Ma according to Matthews et al. (2016) the Philippine Sea plate translated westward and subducted under the Eurasian margin forming the Philippines Sea (PS) slab (Fig. 5a). By 9 Ma the PSCS plate was completely subducted and formed a low-temperature anomaly in the upper mantle (Fig. 5a).

At 0 Ma model 1a predicted a present-day mantle structure that was characterized by three distinct slabs (Fig. 5a): (1) SUN slabs, located above 1000 km depth beneath Java trench; (2) S-PSCS slabs, subducted between 30-15 Ma, located at ~400-800 km depth beneath Borneo; (3) P-PS slabs at ~1000 km depth and another PS slabs at ~400-500 km depth beneath northern SCS. Because our choice of a temperature-dependent Newtonian viscosity is not conductive to a sharp slab break-off (see section 2.2), slabs tend to remain connected to the overlying plate while necking. The present-day temperature field was converted to P and S wave velocities (Fig. 5b) following (Schuberth et al., 2009). This seismic structure was subsequently filtered using the resolution operators of LLNL-G3D (Fig. 5c) and S40RTS (Fig. 5e). The resolution operator of LLNL-G3D does not introduce major artefacts in our study region (cf. Fig. 5b, c). In contrast, filtering the seismic structure generated by the geodynamic model with the resolution operator of S40RTS causes the PS slabs anomalies at ~400-500 km depth beneath northern SCS to

disappear, which suggests S40RTS has limited and biased resolution beneath the SCS region (Fig. 5e). Therefore, for brevity we limit documentation of tomographic filtering for subsequent models to the LLNL-G3D P-wave filter (e.g. Fig. 5c). Comparison of our filtered geodynamic model to the actual LLNL-G3D seismic tomography model (Figs. 5c, d) shows a good match for the SUN slab and S-PSCS slabs beneath Borneo; however, we observe a poor match for the slabs beneath SCS (Fig. 5d).

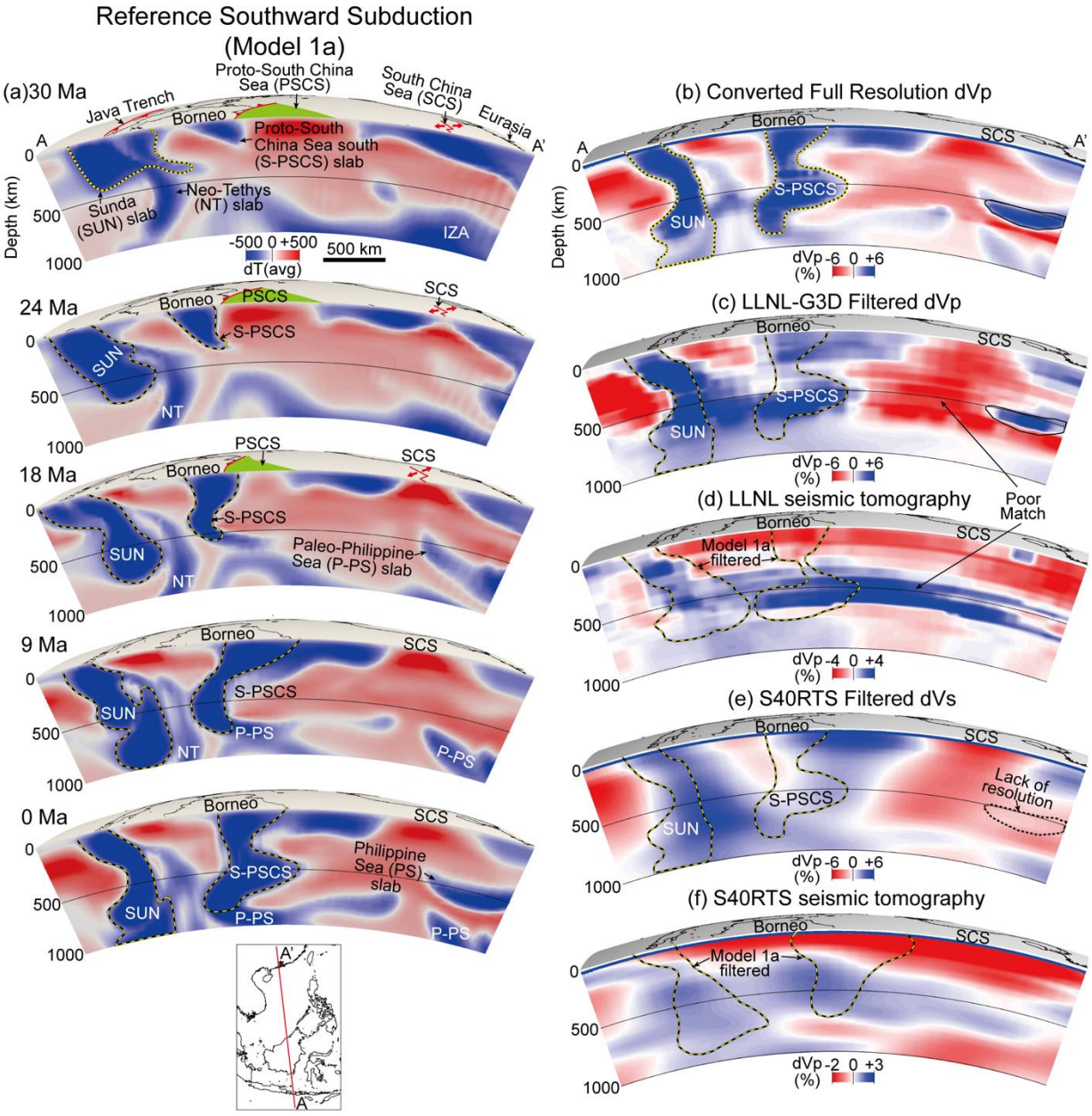

439

440 **Figure 5.** Results of the reference Model 1a that implemented southward PSCS subduction. (a)
441 3D visualizations of the time-dependent mantle thermal structure evolution for the reference
442 southward subduction model 1a from 30 to 0 Ma. The top surface shows the PSCS in green and
443 reconstructed Borneo coastlines. At 0 Ma (present-day), the southward-subducted proto-South
444 China Sea (S-PSCS) slabs are located at ~400-800 km depths beneath Borneo. (b) The 0 Ma
445 temperature field from a) converted to a full-resolution P-wave perturbation (dVp) following
446 Schuberth et al. (2009). (c) Cross-section in (b) filtered through the LLNL-G3D resolution
447 operator (Simmons et al., 2019) to show a 'synthetic tomography' of the 0 Ma geodynamic
448 model. (d) Comparison to section co-located to (c) from actual LLNL-G3D-JPS P-wave seismic
449 tomography model (Simmons et al., 2016). The Sunda (SUN) slabs are generally reproduced but

a mismatch exists under the present SCS. (e) S40RTS resolution operator (Ritsema et al., 2011) was applied to (b). The cold slabs under the northern SCS in b) are not seen in e), indicating lack of resolution in these areas. (f) Comparison of (e) to actual S40RTS S-wave seismic tomography model (Ritsema et al., 2011). The comparison between predicted and imaged mantle structure from S-waves shows the Sunda slabs are generally reproduced but a mismatch exists under the SCS, similar to the P-wave comparison in (c) and (d).

Reference model 1b: double-sided proto-South China Sea subduction

The reference model 1b assimilated a slightly-modified (Matthews et al., 2016) global plate model that was identical to model 1a but implemented a double-sided PSCS subduction (Fig. 6). The cross-sections shown in Figure 6 are co-located with the A-A' transect shown for model 1a in Figure 5. Following our approach, Model 1b had the same 30 Ma initial state as model 1a but the PSCS subduction history diverged after 30 Ma. Between 30 and 15 Ma, SCS spreading drove subduction of the northward-subducted proto-South China Sea north (N-PSCS) slabs under the southward-moving Dangerous Grounds (Fig. 6a); concurrently, imposed Borneo counter-clockwise rotation after 25 Ma (Fig. 3c) produced southward-subducted S-PSCS slabs subduction under NW Borneo (Fig. 6a). Model 1b had a shorter S-PSCS subduction history than model 1a because the PSCS was identical, but was subducted from both the north and south (i.e. double-sided subduction). At 0 Ma model 1b predicted a present-day mantle structure characterized by two sets of PSCS slabs: (1) N-PSCS slabs at ~400-500 km depths beneath southern SCS and NW Borneo; and, (2) S-PSCS slabs at ~400-800 km depths in the mantle beneath Borneo (Fig. 6a). The temperature fields were converted to full resolution dVp (Fig. 6b) and the LLNL-G3D (Fig. 6c) resolution operator was applied. Similar to model 1a (Figs. 5c, d), the LLNL-G3D filtered dVp was relatively comparable to the converted dVp (Fig. 6c), showing

adequate tomographic resolution. Comparing LLNL-G3D filtered model with LLNL-G3D seismic tomography model (Fig. 6c, d) shows a good match for the Sunda slabs similar to Model 1a (Fig. 5). Our modeled PSCS slabs (S-PSCS and N-PSCS slabs) explain a larger portion, but not all, of the fast tomographic anomalies under the SCS slabs beneath Borneo (Fig. 6d) relative to Model 1a (Fig. 5d). Thus, we further investigated PSCS geodynamics by assimilating the refined Model 2 plate models below.

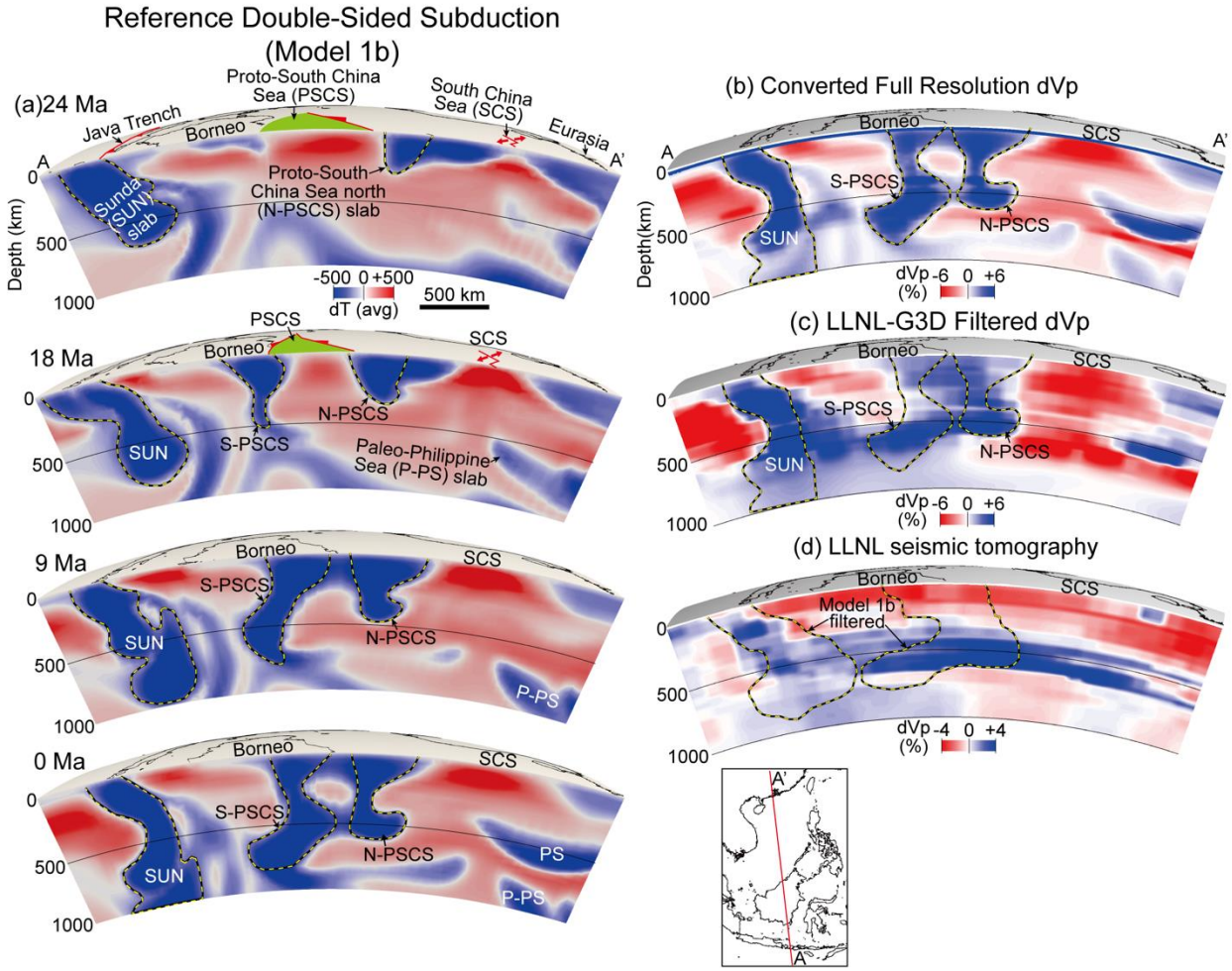

Figure 6. Results of the reference Model 1b that implemented a similar input plate model to Model 1a but invoked double-sided PSCS subduction. (a) 3D volume of the mantle thermal structure evolution from 24 to 0 Ma. The top surface shows the PSCS in green and

reconstructed Borneo coastlines. At 0 Ma, the predicted present-day S-PSCS is at ~400-800 km depths beneath Borneo and the northward-subducted PSCS slabs (N-PSCS) is at ~400-500 km depths beneath the southern SCS. (b) The temperature field from a) at 0 Ma converted to dVp following Schuberth et al. (2009). (c) Cross-section in (b) filtered through the LLNL-G3D resolution operator (Simmons et al., 2019). (d) Comparison of c) to actual LLNL-G3D-JPS P-wave seismic tomography model (Simmons et al., 2016) across the same location. The SUN slabs are generally reproduced in the geodynamic model but the sub-horizontal slabs under the SCS do not match well to the geodynamic model.

Model 2a and Model 2b: refined southward PSCS and double-sided PSCS models

Figure 7 shows the end-state of models 2a and 2b and a comparison to global P-wave seismic tomography models. Models 2a and 2b began from the 45 Ma state of the default model 0 (Fig. S2) and implemented the refined 'southward proto-South China Sea subduction' and 'double-sided proto-South China Sea subduction' plate models (Figs. 4c, d), respectively. The time evolution of models 2a and 2b from 42 Ma is shown in the supplemental Figure S3. Models 2a and 2b show a broadly similar evolutionary history relative to the reference models 1a and 1b (compare Figs. 5,6, S3) except that the Philippine Sea slab within the transition zone, seen in models 1a and 1b (Figs. 5, 6), was not produced in models 2a and 2b (Fig. 7). This was due to our assimilation of a much smaller Philippine Sea plate (Fig. 3f).

The final model state is presented in Figures 7a and b along transect B-B', which was nearby C-C' in Figure S1 and best shows the model differences. At 0 Ma, both models 2a and 2b produced the southward-subducted S-PSCS slabs at ~400-1000 km depths beneath Borneo (Fig. 7a, b). However, as expected the refined double-sided model 2b also produced northward-subducted N-PSCS slabs; the N-PSCS formed a sub-horizontal swath of slabs under the present SCS at 500

512 to 700 km depths. LLNL-G3D resolution operator filtered reference models 1a and 1b show that
513 these broad mantle structures are generally preserved after filtering (Figs. 5, 6); therefore, in
514 Figure 7 we show a direct comparison between the full temperature field and the three global
515 P-wave seismic tomographic sections (Figs. 7c to e). Both models 2a and 2b and the actual
516 seismic tomography models show relatively well-reproduced SUN slabs (Fig. 7). The S-PSCS
517 slabs possibly correlate to shallow, lower amplitude tomographic anomalies within the
518 transition zone and higher amplitude anomalies below 700 km depths under NW Borneo in
519 UUP07 (Amaru, 2007) and GAP_P4 (Fukao & Obayashi, 2013) seismic tomography models, but
520 the shallow anomalies are absent in MITP08 (Li et al., 2008) seismic tomography models (Fig. 7).
521 Finally, the N-PSCS slabs that were uniquely produced in model 2b yield a markedly better fit to
522 the sub-horizontal slabs in the mantle transition zone under the present SCS, although the
523 tomographic anomalies seem to extend a bit further north than the geodynamic models (Figs.
524 7b to e).
525

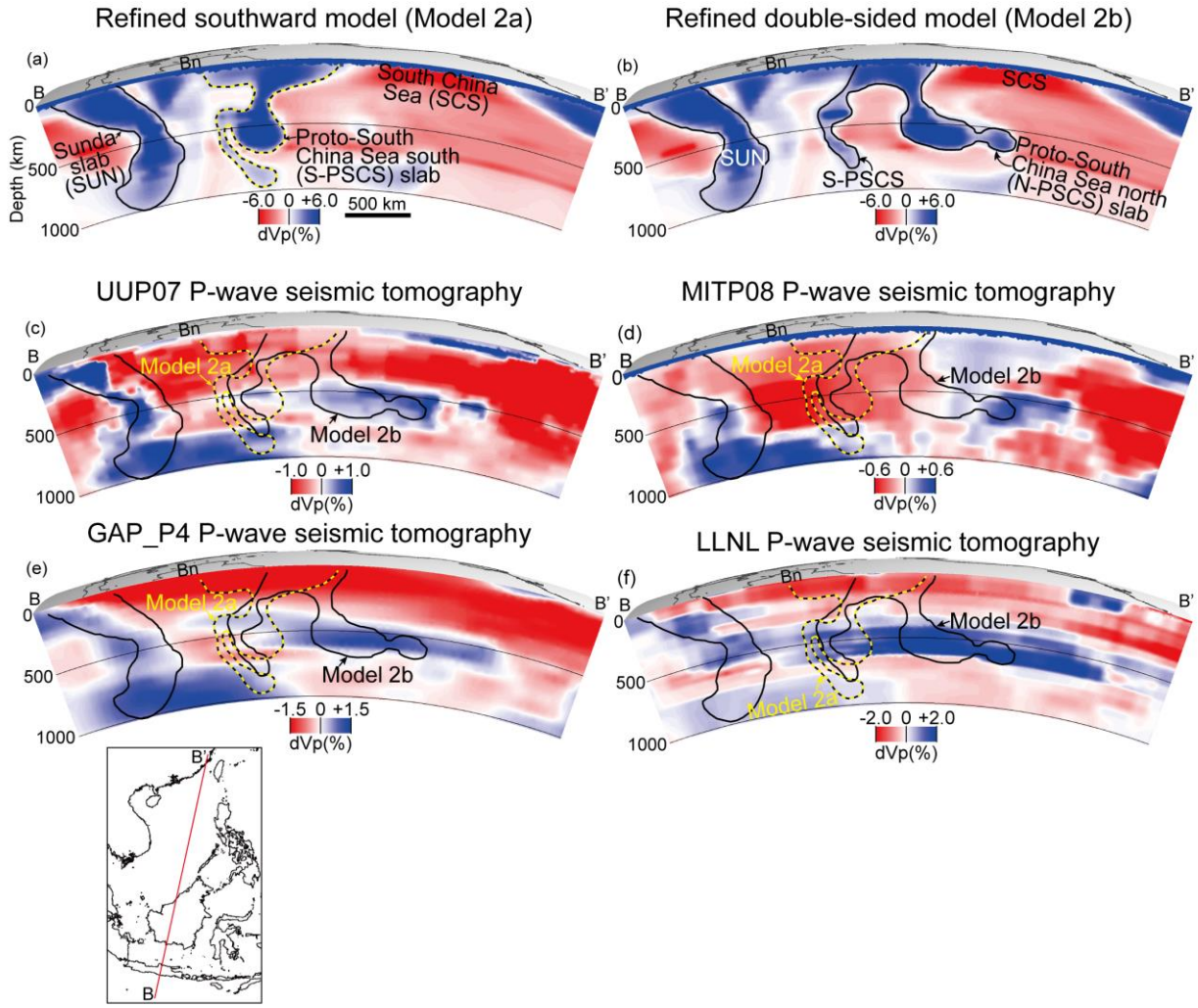

Figure 7. Geodynamic model results for our refined models 2a and 2b. The top surface shows present coastlines for reference. (a) Final 0 Ma mantle structure predicted from the refined southward subduction model 2a shows the southward-subducted S-PSCS slabs at ~400-1000 km depths beneath Borneo. (b) In contrast, the refined double-sided model 2b shows S-PSCS slabs at ~400-1000 km depth beneath Borneo and northward-subducted N-PSCS slabs at ~500-700 km depths beneath the southern SCS. Comparison between global P-wave seismic tomography models (c) UUP07 (Amaru, 2007), (d) MITP08 (Li et al., 2008), (e) GAP_P4 (Fukao & Obayashi, 2013), and (f) LLNL-G3D-JPS (Simmons et al., 2016) and the geodynamic models (yellow and black outlines) across B-B'. The N-PSCS slabs in Model 2b shows a better match to the sub-horizontal slabs under the present SCS in tomography at 400 to 700 km depths. Bn: Borneo.

4. Discussion

4.1 Comparison between geodynamically-modeled and seismically-imaged mantle structure

We discuss the implications of each plate model for mantle structure by comparing the predicted mantle structure from our geodynamic models against tomographically-imaged mantle structure. Before comparing the geodynamic models with seismic tomography model, we first investigated the consistency between multiple P-wave tomography models under Southeast Asia, including MITP08 (Li et al., 2008), GAP_P4 (Fukao & Obayashi, 2013), UUP07 (Amaru, 2007) and LLNL-G3D-JPS (Simmons et al., 2015), and S-wave models, including LLNL-G3D-JPS (Simmons et al., 2015) and S40RTS (Ritsema et al., 2011) (Fig. 8a). The correlation coefficient between various seismic tomography models at 400-600 km depth in the study area was ~0.2 to 0.7, indicating a reasonable consistency (Fig. 8a). The highest correlation coefficients (between 0.69 to 0.71) were observed between the global P-wave seismic tomography model MITP08, UUP07 and GAP_P4 (Fig. 8a). Since these three models are commonly used for Southeast Asian mantle studies (e.g. Hall & Spakman, 2015; Zahirovic et al., 2016), we chose to combine the three tomography into a fast-anomalies vote map (Hosseini et al., 2018; Shephard et al., 2017) to simply the comparison between the geodynamic models and tomographic imaging described below (Fig. 8b, c).

Correlations between our geodynamic models and the seismic tomography model MITP08, GAP_P4, UUP07 are about 0.08 to 0.24 in this region (Fig. 8a). These correlations are not high but are comparable to global scale average correlations of degree 1-20 (Shephard et al., 2012); thus, we conclude the geodynamic modeling strategy used here can adequately reproduce

seismically-imaged mantle structures, to the first order. The major regional feature that is robustly imaged by all tomographic models is a swath of fast Sunda (SUN) slab anomalies beneath Peninsular Malaysia, Sumatra and Java; all geodynamic models are able to reproduce these anomalies (Fig. 8b, c). On the other hand, all tomographic models image N-S trending anomalies beneath Celebes Sea that are not reproduced by any of the four geodynamic models (Fig. 8b, c). This suggests that the assimilated plate models need further improvements in these regions (i.e. Molucca Sea), which is not surprising given current debates (Hall & Spakman, 2015; Wu et al., 2016; Zahirovic et al., 2016).

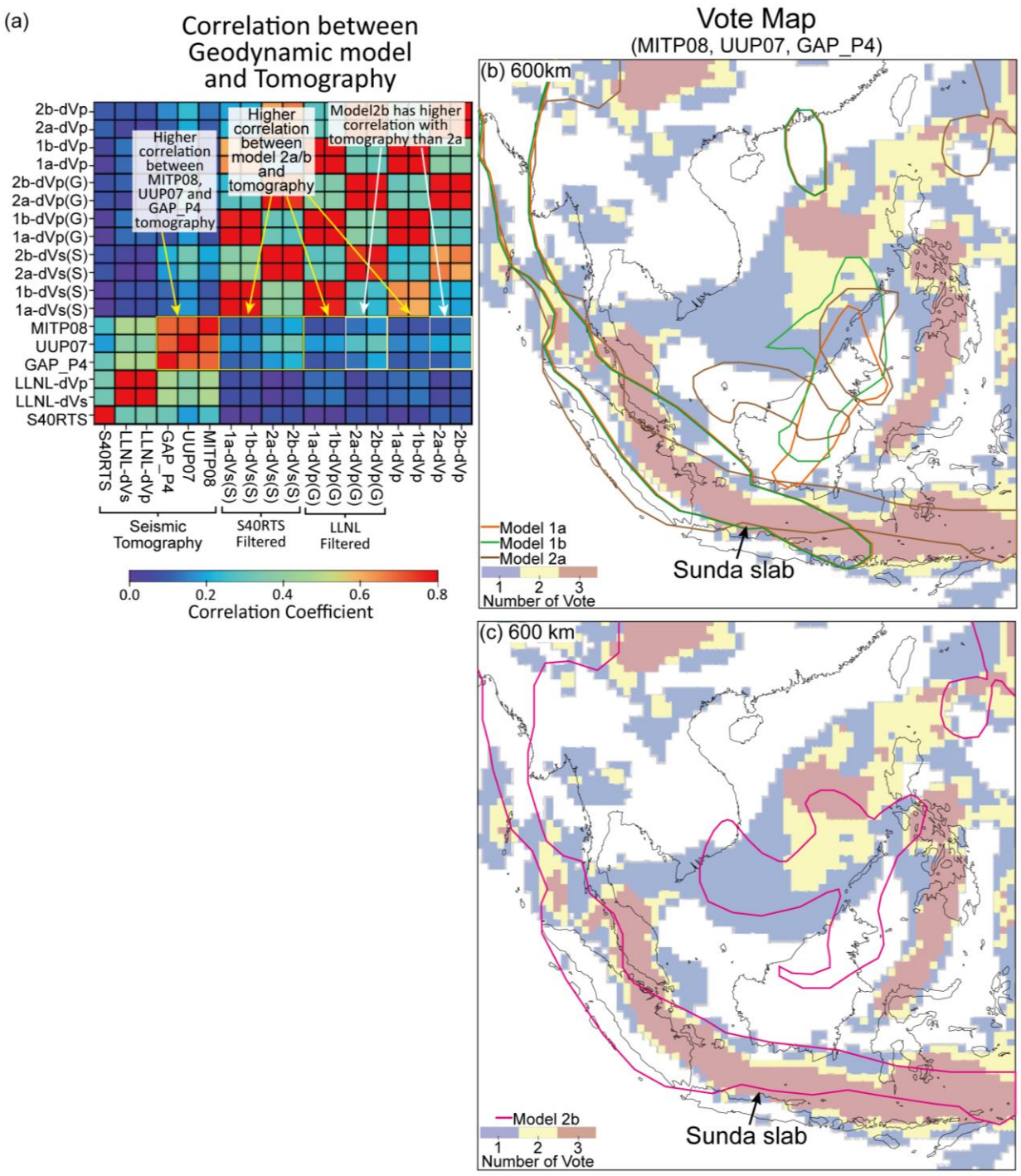

571

572 **Figure 8.** Comparison between geodynamic model results and tomography. (a) Color-coded
573 correlation coefficient matrix showing similarities between various geodynamic models, seismic
574 tomography models, and geodynamic models v.s. seismic tomography models at 400-600 km
575 depths. Models 2a and 2b show higher correlations to seismic tomography models relative to
576 Models 1a and 1b. The global P-wave seismic tomography models MITP08 (Li et al., 2008),
577 GAP_P4 (Fukao & Obayashi, 2013) and UUP07 (Amaru, 2007) show ~0.6-0.8 correlations
578 relative to each other. The correlation between geodynamic models and seismic tomography

models is ~0.2 correlation, which is comparable to global averages for degree 1-20 (Shephard et al., 2012). (b), (c) show fast-anomaly vote maps from MITP08, GAP_P4 and UUP07 seismic tomography model at 600 km depths in comparison to b) Models 1a, 1b, and 2a, and (c) our preferred model 2b. Color lines indicate the fast anomalies from the full resolution, dVp-converted geodynamic model results. All models generally reproduce the Sunda slabs. Model 2b was able to better reproduce the slabs under the present SCS in (b) and (c). Model-dVp: full resolution dVp; Model-dVs(S): S40RTS resolution filtered dVs; Model-dVp(G): LLNL-G3D resolution filtered dVp

Models 2a and 2b achieved a higher degree of correlation (~0.10-0.24) with seismic tomography model compared to models 1a and 1b (~0.08-0.16) (Fig. 8a). Models 2a and 2b were able to better reproduce the fast anomalies beneath the Banda arc and offshore from the Ryukyu trench (Fig. 8b, c), due to the alternative plate boundary geometries and subduction zones introduced by assuming a smaller Philippine Sea plate, and by filling the resulting gap between it and Eurasia with a marginal basin (cf. Fig. 3e-f).Moreover, as the marginal sea is overridden by the Philippine Sea plate, it generates a shallow-dipping slab (labeled 'vanished ocean; in Fig. S7) that provides superior fit to fast anomalies in the mantle beneath Philippine Sea at ~600 km depth imaged by MITP08, LLNL-G3D-JPS and S40RTS seismic tomographic models (Fig. S7). A number of studies have argued for reconstructing the Philippine Sea plate as a smaller plate with a shorter (~1000 km) subducted northward extent (Fig.3f) (Deschamps & Lallemand, 2002; Hall, 2002; Wu et al., 2016); our models show this is a more viable scenario than other proposed models that invoke a much larger Philippine Sea plate (Fig. 3e).

4.2 Where are the PSCS slabs?

Many contrasted PSCS slab interpretations have been proposed based on various seismic tomography model (Fig. 2d). By exploring various contrasted plate models through geodynamic modeling, we are able to provide some insight toward the possible present locations of the PSCS slabs. The four plate models assimilated in this study represent very different PSCS subduction histories, Borneo rotations, and Philippine Sea plate reconstructions within global geodynamic models (Fig. 3) (see section 2.1). This allows us to investigate a range of possible PSCS slab locations in the mantle for the first time (Fig. 9). Our models generally produced PSCS slabs between 500 to 800 km depths under eastern Borneo, the present SCS the Sulu and Celebes seas, and the southern Philippines (dotted black lines in Fig. 9). Thus, we consider these areas to be the most likely locations for the PSCS slabs.

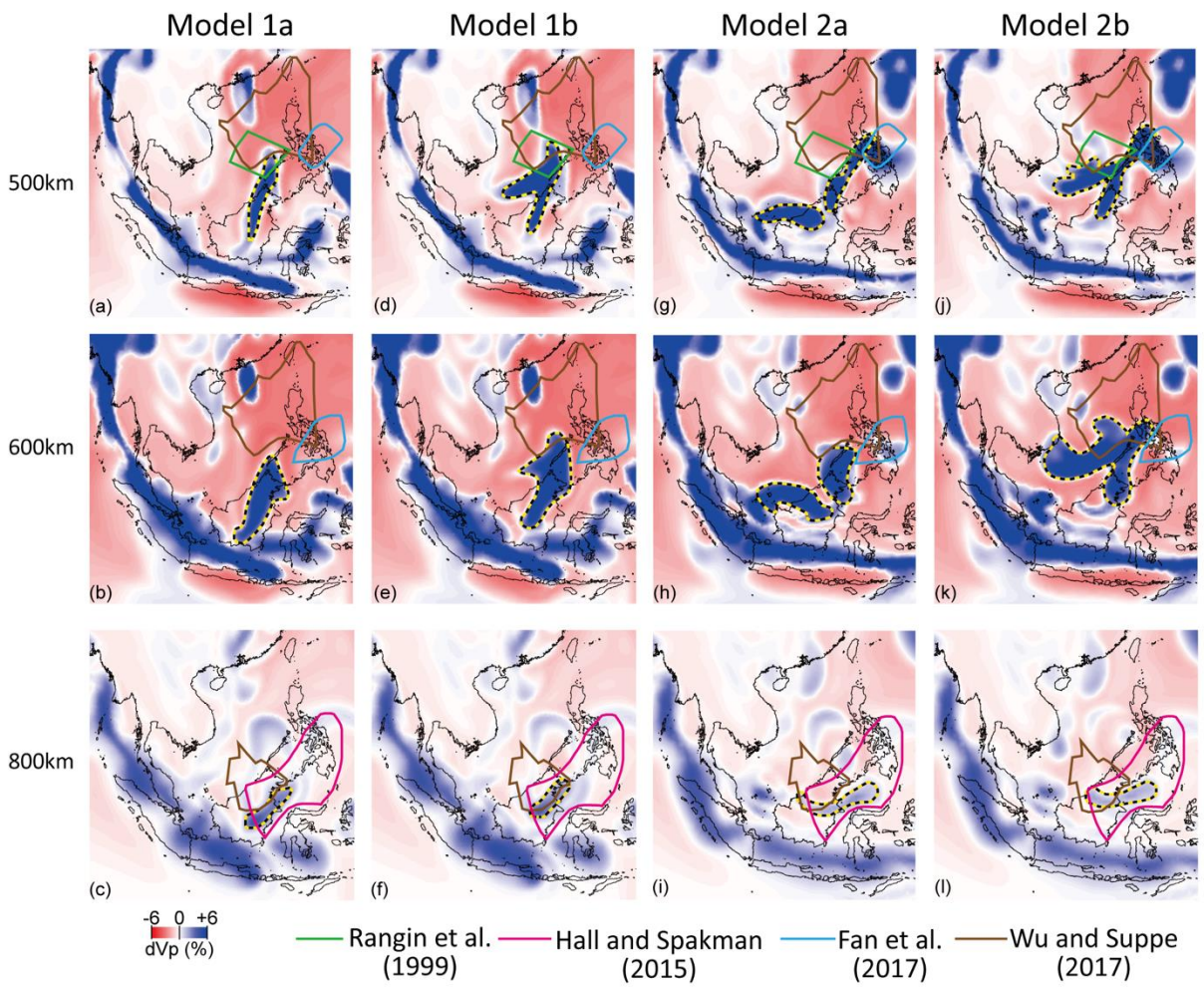

615

616 **Figure 9.** Locations of predicted and interpreted proto-South China Sea (PSCS) slabs within the
617 SE Asian mantle shown by maps of the full resolution, dVp-converted geodynamic model results
618 horizontal sections at 500, 600 and 800 km depths. (a) to (c) show Model 1a, (d) to (f) Model 1b,
619 (g) to (i) Model 2a, and (j) to (l) Model 2b. Locations of PSCS slabs interpreted from tomography
620 by previous studies are shown by the colored polygons. Black dashed lines indicate the PSCS
621 slabs predicted from geodynamic models. When all four models are considered together, our
622 geodynamic models generally predict the PSCS slabs are under Borneo, the present SCS, the
623 Celebes Sea, and the Philippines between 500 to 800 km depths.
624

625 As expected, our modeled PSCS slab locations varied according to the input plate tectonic

626 models. For example, counter-clockwise (CCW) Borneo rotations between ~24-11 Ma (Fig. 3c)

627 produced PSCS slabs beneath Palawan and Borneo, striking SSW-NNE (model 1a, Fig.9a-c black

628 dashed lines). The double-sided subduction model (model 1b) produced a similar PSCS slabs

629 and generated additional PSCS slabs offshore NE Borneo and Palawan due to northward PSCS
630 subduction (Fig. 9d to f). The alternative Borneo rotation in our refined models (35°CCW
631 rotations during 45-34 Ma and ~10°CCW during 23-16 Ma; Fig. 3c) shifts the PSCS south slabs
632 slightly northwards and eastwards, and adds some PSCS south slabs to the southwest (Fig. 9g-i
633 black dashed lines). The refined double-sided subduction model (model 2b, see Fig. 3d)
634 produced slightly different PSCS south slab locations at 500 and 600 km depths that reduced
635 overall slab volumes beneath eastern Borneo (compare Figs. 9g to l). The double-sided
636 subduction also produced a swath of PSCS north slabs trending WSW-ENE between offshore
637 southern Vietnam towards the Philippines (Fig. 9j-I black dashed lines).
638
639 *Comparison to published PSCS slab interpretations*
640
641 Fan et al. (2017) interpreted fast tomographic anomalies at 400-700 km depth beneath central
642 Philippines as PSCS slabs that were generated by southward subduction of a narrow PSCS ocean
643 basin. Our diverse models produced slabs under the central Philippines from various sources:
644 subducting a vanished ocean, a large Philippines Sea plate, or the PSCS (Fig. 9a, b ,g, j);
645 therefore, some caution is needed when inferring the plate tectonic histories of slabs under the
646 central Philippines. Hall and Spakman (2015) interpreted PSCS slabs from fast velocity
647 anomalies within UUP07 tomography model at ~800 km depths between eastern Borneo and
648 the southern Philippines (Figs. 9c, f, i, l). These PSCS slabs were attributed to southward PSCS
649 subduction between ~45 to 20 Ma (Hall & Spakman, 2015). Other seismic tomography models
650 also show slabs at 800 km depths under the southern Philippines (Fig. S6) that support the

651 UUP07 seismic tomography model of Hall and Spakman (2015). Our geodynamic models
652 produced PSCS slabs at 800 km depths beneath central Borneo but these slabs did not extend
653 eastwards under the southern Philippines (Figs. 9c, f, i, l). However, our plate models did not
654 implement a PSCS subduction zone as far east of Borneo as Hall (2012); therefore, we cannot
655 exclude the possibility of PSCS slabs being present beneath eastern Borneo and extending east
656 of the southern Philippines.
657
658 Wu and Suppe (2018) identified sub-horizontal, fast anomalies in the upper mantle beneath the
659 SCS and interpreted these to be PSCS (Fig. 2d). Rangin et al. (1999) also interpreted the
660 southernmost tomographic anomalies described above as PSCS, but did not continue their
661 analyses further northwards. The other tomographic models considered here also show these
662 fast anomalies (Figs. 7c to f). Only the double-sided PSCS subduction plate models (model 2b)
663 reproduced the fast anomalies underneath the SCS (Fig. 7b, 8c and S6), suggesting that double-
664 sided PSCS subduction is viable. On the other hand, none of our modeled slabs under the
665 present SCS extend as far north as the imaged fast anomalies (Fig. 7c to f). Part of the
666 difference in morphology and dip of the slabs can be explained by the limitations of our
667 geodynamic models to produce an abrupt slab break-off, and thus, a flatter-lying slab. The
668 latitudinal extent of slab material at these depths, instead, is only weakly controlled by our
669 choice of geodynamic parameters. The imposed history of plate motions has a more direct
670 effect; as such, a better match could be achieved in principle by imposing a more northerly
671 position of the PSCS and all associated Southeast Asian subduction zones (i.e. mantle reference).
672 This, however, would contradict paleomagnetic data on the best-fit paleo-position of Borneo

673 (Advokaat et al., 2018; Fuller et al., 1999). Moreover, it would require adjustments to the paleo-
674 location of the Sunda trench, which was successfully reproduced by all models (Fig. 8b, c).
675
676 *4.3 Implications for PSCS plate tectonic reconstructions*
677
678 *Southward vs. Double-sided PSCS subduction*
679
680 Conventional Southeast Asian plate models typically show southward subduction of the PCSC
681 under north Borneo (Fig. 2a) (Holloway, 1982; Taylor & Hayes, 1983). The geodynamic models
682 in this study confirm that southward PSCS subduction cannot by itself fully reproduce Southeast
683 Asian mantle structure, and in particular, the sub-horizontal slabs under the present SCS at 400
684 to 700 km depths (compare Fig. 7a to 7c-f). Similar results have been shown by previous
685 geodynamic models (Zahirovic et al., 2016) but were not fully-described. Instead, we show for
686 the first time that the double-sided PSCS subduction model (Fig. 2b) (Wu & Suppe, 2018)
687 produces a better match to tomographically-imaged mantle structure (compare Fig. 7b to 7c-f)
688 than southward PSCS subduction only. On the other hand, the match of our preferred double-
689 sided PSCS subduction model 2b and seismic tomography model is far from perfect (Fig. 7);
690 maximum correlation coefficients are ~0.24 (Fig. 8a). There is scope for future studies to further
691 improve the fit between geodynamic and seismic tomography model. Furthermore, it is
692 acknowledged that additional geological evidence is needed to support double-sided PSCS
693 subduction, including a second volcanic arc to account for the northern SCS subduction zone
694 (Wu & Suppe, 2018). Indeed, a recent review of the SCS geology concluded that double-sided

PSCS subduction is less consistent with current geological constraints (Zhang et al., 2019). It is widely agreed that NW Borneo and the SCS itself have an enigmatic tectonic history (e.g. Sun et al., 2019; Wang et al., 2019; Zhao et al., 2019); thus, it is recommended that future geological studies should further test the proposed double-sided PSCS model. In summary, our results indicate a preference for double-sided PSCS subduction (Fig. 2b) but the southward PSCS subduction model (Fig. 2a) cannot be excluded simply on the basis of a poorer fit to mantle structure (Fig. 7). Nonetheless, for the purposes of the following sections we will consider the double-sided PSCS subduction model 2b as our preferred model.

Extrusion model

Although this study did not explicitly assimilate the extrusion model (see review in 1.1) (Tapponnier et al., 1982), the extrusion model is somewhat testable from our results because of its mantle structure implications, including (Fig. 2c): (1) significant Sunda trench rollback occurred since the Eocene; and, (2) PSCS slabs should not exist under Southeast Asia. All plate models implemented in our geodynamic models did not include significant Sunda trench rollback, and in some cases, implemented limited trench advance (Fig. 2; see also the plate model animations). However, all our models produced a satisfactory match to the Sunda slabs (Figs. 7, 8b, c), suggesting that major SE extrusion is unnecessary to generate a fit to mantle structure. Regarding the existence of PSCS slabs, our model 2b generally reproduced the fast tomographic anomalies under the present SCS and Borneo by implementing a double-sided PSCS subduction history (Figs. 7b to f). Therefore, our results seem to favor the existence of a

PSCS (Figs. 2a, b). Again, this suggests that major SE extrusion (Fig. 2c) is unnecessary with regards to fitting Southeast Asian mantle structure. On the other hand, we did not explicitly test 'hybrid' models that invoke a combination of limited extrusion and a smaller PSCS (e.g. Cullen, 2010). Although a hybrid model could be viable, it is yet unclear how subduction of a far smaller PSCS could generate enough subducted lithosphere (i.e. slabs) to account for the many slab-like, fast anomalies under Borneo and the SCS (Fig. 7c to f).

4.4 Predicted mantle flow and its implication

Mantle flows under Indochina during late Eocene to Oligocene times

Our methodology allows us to make explicit predictions not only for the present-day state of the mantle but also for its past evolution. However, we limit our current analysis to the Cenozoic because modeled flow becomes increasingly dependent on the unknown initial condition as one looks further back into the past (Colli et al., 2015; Colli et al., 2020). Mantle flow underneath Southeast Asia depends on the details of the input plate model, as shown by our results (Fig. S8). Underneath the northern part of Indochina and the SCS, instead, all four models generated a similar mantle flow in this region since the input plate models differ only locally (Fig. S9, S10). Focusing on model 2b, our results show a passive return-flow upwelling from mid-mantle depths beneath Hainan island and Indochina in late Eocene to Oligocene (Fig. 10a, b, S9) induced by the interaction between the long-established subduction zone surrounding Southeast Asia and recent spreading in the SCS. This upwelling, while not being

739 rooted at the core-mantle boundary, is still sourcing lower mantle material and may be
740 sufficient to explain the OIB-like component of the Eocene-Oligocene magmatism around
741 Indochina and South China (Liu et al., 2017; Zhang & Scharer, 1999; Zhou et al., 2009).
742 Furthermore, the upwellings predicted by our models provide a possible explanation for the
743 well-documented but poorly-explained 'syn-rift'-style sedimentary sequences recorded within
744 most Sundaland sedimentary basins (Pubellier & Morley, 2014).
745
746 *Hainan plume*
747
748 A number of studies have debated the existence of a deep mantle-origin plume under South
749 China, named the Hainan plume (e.g. Lei et al., 2009). Our results predict sub-horizontal E-W
750 directed flow in the upper mantle during late Miocene to present-day underneath Northern
751 Indochina and South China (Fig. 10c, d), in agreement with regional shear wave splitting
752 directions (Chang et al., 2015; Yu et al., 2018). These mantle flow patterns were robustly
753 predicted in spite of plate model variations (Fig. S10). Therefore, our results do not support a
754 deep-mantle and high-temperature origin for Miocene magmatism (so-called 'Hainan plume')
755 (Kimura et al., 2018; Lebedev & Nolet, 2003; Lei & Zhao, 2006; Wang et al., 2013). Instead, we
756 would suggest that smaller-scale processes such as local extension shear-driven upwelling
757 (Bianco et al., 2011; Conrad et al., 2011) may have generated melt from ambient mantle which
758 then migrated through zones of weakness in the lithosphere to produce the regional
759 magmatism.
760

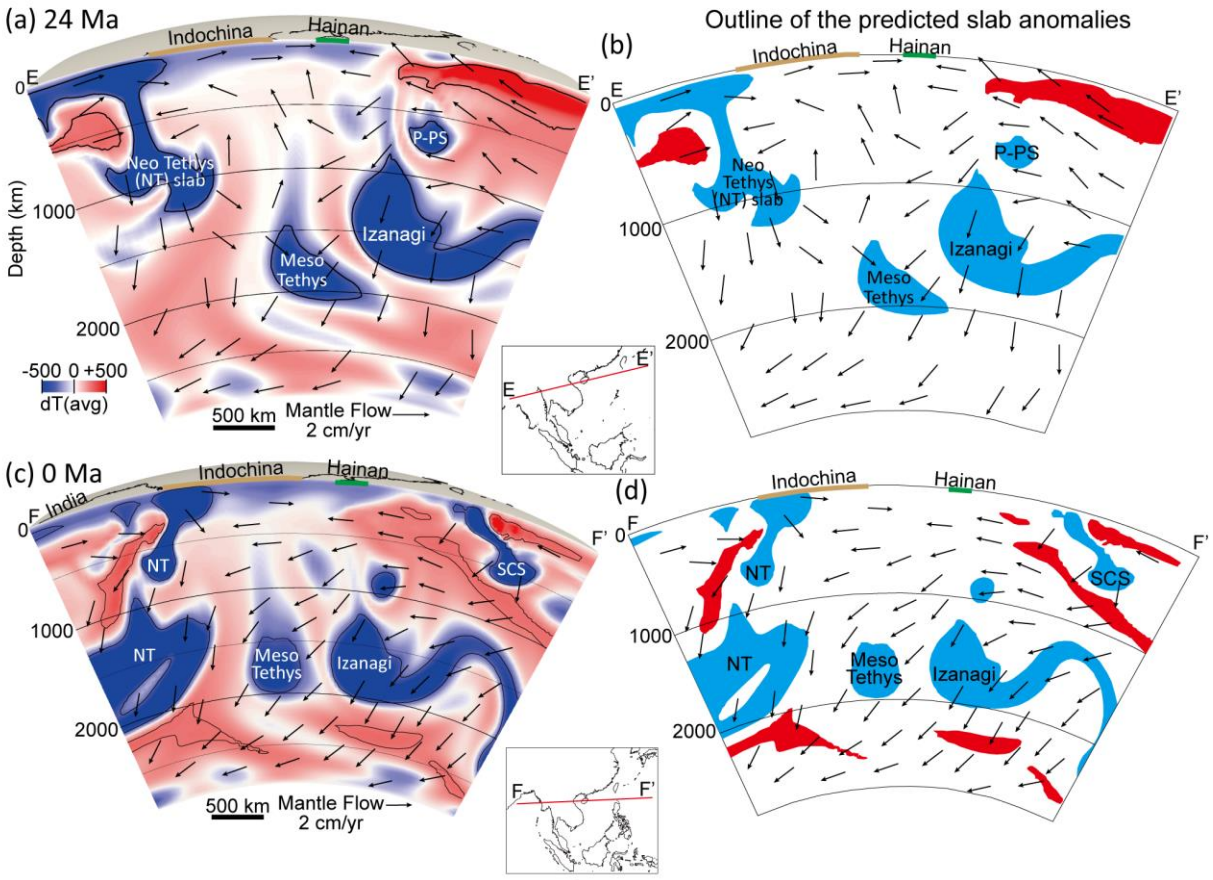

Figure 10. Predicted mantle flows and mantle structures from our preferred geodynamic model 2b under Indochina and Hainan Island during (a) to (b) the latest Oligocene 24 Ma, and, (c) to (d) present-day 0 Ma. From the late Eocene to Oligocene we predict a mid-mantle convective upwelling beneath Indochina and Hainan. At 0 Ma, we predict an extensive E-W directed mantle downwelling that are inconsistent with the proposed deep-origin Hainan mantle plume. Black arrows show mantle flows and the black lines indicate the +/-300°C temperature contours. The inset maps show reconstructed coastlines and cross-section locations at 24 Ma and the present-day.

Dynamic topography

The implementation of multiple Southeast Asian plate models into our geodynamic models allow us to investigate for the first time the effects of alternative plate tectonic histories on Sundaland dynamic topography. Dynamic topography within Sundaland (i.e., topography

776 generated by mantle convection) is important because the broad, low-lying continental
777 landmass is susceptible to flooding, and this has implications for climate, biogeography, and
778 sedimentary basin evolution (Sarr et al., 2019; Yang et al., 2016; Zahirovic et al., 2016).
779 However, Sundaland dynamic topography is challenging to analyze because uplift and
780 subsidence has also occurred due to active tectonics. The tectonic evolution of Sundaland
781 during the Cenozoic has been divided into three main phases (Doust & Sumner, 2007):
782 widespread extension and syn-rift subsidence during the Paleogene; tectonic quiescence and
783 thermal subsidence in Early Miocene; widespread compression, inversion and uplift in Middle
784 Miocene to Recent. Most basins experienced maximum transgression during Early Miocene,
785 followed by a regressive phase. Yang et al. (2016), however, argued that the combined effect of
786 basin inversion and contemporaneous long-term eustatic sea level fall (Haq & Al-Qahtani, 2005)
787 should have resulted in a much stronger regressive phase. They thus concluded that an
788 additional component of subsidence, due to temporal variations of dynamic topography, is
789 needed to explain the mild amplitude of the regressive phase and the backstripped subsidence
790 curves of a number of Sundaland basins. The structural and thermal components of subsidence
791 and uplift can be quantified directly from the amount of extension and compression in space
792 and time (i.e., strain rates) using simple models of isostasy and thermal conduction (e.g. Jarvis
793 & McKenzie, 1980b). Unfortunately, the majority of Sundaland structural deformation cannot
794 be constrained with sufficient precision. Indeed, Yang et al. (2016) obtained lithospheric
795 deformations using a new inverse method. They first computed a history of dynamic
796 topography using a numerical model of mantle convection. They then subtracted it from the
797 observed backstripped tectonic subsidence curves of a number of Sundaland basins, and finally

798 inverted this residual subsidence for best-fitting lithospheric deformation. This inverse
799 methodology is theoretically sound but requires well-constrained predictions of dynamic
800 topography variations. Our results show that such predictions are highly sensitive to the
801 imposed history of surface plate motions (Fig. 11a). Regions of complex and poorly constrained
802 tectonic motions such as Southeast Asia are thus poorly suited for the inverse methodology of
803 Yang et al. (2016).
804
805 We finally focus on the Cuu Long basin, as it is one of the few basins in Sundaland to experience
806 little to no Miocene inversion (Doust & Sumner, 2007), making it particularly well-suited for
807 subsidence analysis. Following Jarvis and McKenzie (1980b) we use the syn-rift part of the
808 subsidence curve (34-24 Ma, Doust & Sumner, 2007) to estimate total deformation and the
809 thermal component of post-rift subsidence (a complete list of modeling parameters are listed in
810 table S1). Figure 11b shows that the subsidence curve of the Cuu Long basin requires ~400 m of
811 dynamic uplift in the Neogene. Dynamic uplift is predicted at this location, regardless of input
812 plate model, from a minimum of ~100 m for model 2b to a maximum of almost one kilometer
813 for model 1a, with models 1b and 2a yielding the best match (Fig. 11b). Without additional
814 work, we cannot further pinpoint Sundaland dynamic topography, but our results show for the
815 first time that accurate plate tectonic histories are essential; we find a ~1 km difference in
816 predicted dynamic topography based on the input plate model (Fig. 11b). Therefore, caution is
817 needed for dynamic topography studies that implement only a single plate tectonic history in
818 active tectonic regions that have debated plate tectonic histories. Furthermore, our results
819 suggest the Cuu Long basin should be a key benchmarking area for future studies.

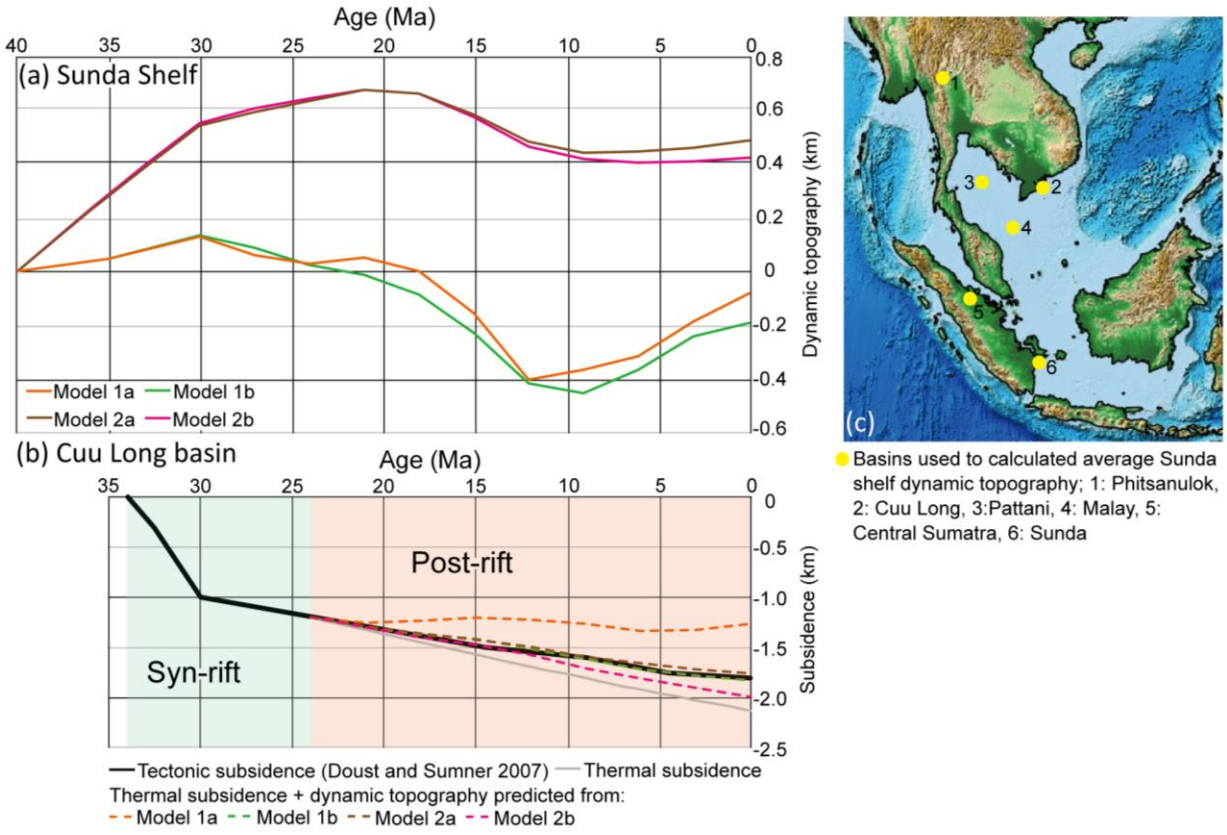

Figure 11. Dynamic topography predicted by the geodynamic models in this study. (a) Models 1a, 1b, 2a and 2b shows highly contrasted dynamic topography histories at Sunda shelf. This suggests that dynamic topography predictions are strongly dependent on the input plate model, which are controversial. (b) Comparison between observed and predicted tectonic subsidence at the Cuu Long basin, offshore Vietnam. (c) Map showing the sedimentary basins used to calculate an average Sunda shelf dynamic topography. At the post-rift stage there is ~400 m vertical discrepancy between the observed tectonic subsidence (black line) and the modeled thermal subsidence (grey line). By adding the predicted dynamic topography to thermal subsidence, we show a better fit the predicted total tectonic subsidence (colored dashed lines). Models 1b and 2a yield the best match to the observed subsidence.

5. Conclusion

Assimilation of kinematic models of past plate motions into geodynamic models of mantle convection lead to specific predictions for the present-day location and morphology of

subducted slab material and for the recent history of mantle flow. Our results show that southward subduction of the PSCS, while being consistent with the geologic record of North Borneo and Palawan, implies the presence of a slab in the upper mantle beneath Borneo and Palawan islands and offshore Palawan islands that is not currently imaged by seismic tomography model. Double-sided PSCS subduction (i.e. both northward and southward PSCS subduction), instead results in a better match against seismic tomographic structure. Nevertheless, the fast anomalies reported by some seismic tomography models in the upper mantle beneath the northernmost part of the SCS are challenging to reproduce even in a double-sided PSCS subduction scenario. Furthermore, our results suggest that a reconstructed smaller Philippines Sea plate (with a shorter ~1000 km north extent) is a more viable case than a very large ~3000 km-long Philippine Sea. In this study we showed that assimilation of locally-contrasted plate models within recent Earth history (since Eocene times) can generate different enough predictions for present-day mantle structure to be testable by global and regional seismic tomography models. This approach can be further applied to areas where the surface geology does not provide a unique constraint (e.g. the hypothesized Resurrection plate along the NW Cordillera during Cenozoic times). We further show that dynamic topography histories within active tectonic regions (e.g. Sundaland) are intimately linked to imposed plate tectonic histories. Thus, where plate tectonic histories are controversial, multiple plate models should be assimilated to consider a range of possible dynamic topography outcomes.

Acknowledgement

We sincerely thank Christian Heine, Eldert Advokaat, Yiduo Andy Liu and our lab members Jeremy Tsung-Jui Wu, Spencer Fuston and Yi-Wei Chen, for valuable discussion and support. Yi-An Lin and Jonny Wu were supported by U.S. National Science Foundation grant EAR-1848327. We also thank Bernhard Schuberth, Nathan Simmons and Thomas Chust for assistance and helpful discussions on mineral physics and tomographic filtering. The authors acknowledge the use of the Opuntia and Sabine Clusters and the advanced support from the Research Computing Data Core at the University of Houston to carry out the research presented here. Lorenzo Colli acknowledges funding provided by the Governor's University Research Initiative (GURI) of the State of Texas. Emerson Paradigm are acknowledged for providing educational licenses of the software Gocad.

References

Advokaat, E. L., Marshall, N. T., Li, S., Spakman, W., Krijgsman, W., & van Hinsbergen, D. J. J. (2018). Cenozoic Rotation History of Borneo and Sundaland, SE Asia Revealed by Paleomagnetism, Seismic Tomography, and Kinematic Reconstruction. *Tectonics, 37*(8), 2486-2512. doi:10.1029/2018TC005010

Amaru, M. L. (2007). *Global travel time tomography with 3-D reference models.* (Doctoral PhD Thesis). Utrecht University, Geologica Ultraiectina. (274)

879 Bai, Y., Wu, S., Liu, Z., Müller, R. D., Williams, S. E., Zahirovic, S., & Dong, D. (2015). Full-fit
880 reconstruction of the South China Sea conjugate margins. *Tectonophysics, 661*, 121-135.
881 doi:10.1016/j.tecto.2015.08.028

882 Bianco, T. A., Conrad, C. P., & Smith, E. I. (2011). Time dependence of intraplate volcanism
883 caused by shear-driven upwelling of low-viscosity regions within the asthenosphere. *Journal of*
884 *Geophysical Research: Solid Earth, 116*(B11), B11103. doi:10.1029/2011JB008270

885 Bunge, H.-P., & Grand, S. P. (2000). Mesozoic plate-motion history below the northeast Pacific
886 Ocean from seismic images of the subducted Farallon slab. *Nature, 405*, 337-340.
887 doi:10.1038/35012586

888 Bunge, H.-P., Richards, M. A., Lithgow-Bertelloni, C., Baumgardner, J. R., Grand, S. P., &
889 Romanowicz, B. A. (1998). Time Scales and Heterogeneous Structure in Geodynamic Earth
890 Models. *Science, 280*(5360), 91-95. doi:10.1126/science.280.5360.91

891 Chang, L.-J., Ding, Z.-F., & Wang, C.-Y. (2015). Upper mantle anisotropy beneath the southern
892 segment of North-South tectonic belt, China. *Chinese Journal of Geophysics (in Chinese), 58*(11),
893 4052-4067. doi:10.6038/cjg20151114

894 Chust, T. C., Steinle-Neumann, G., Dolejš, D., Schuberth, B. S. A., & Bunge, H. P. (2017). MMA-
895 EoS: A Computational Framework for Mineralogical Thermodynamics. *Journal of Geophysical*
896 *Research: Solid Earth, 122*(12), 9881-9920. doi:10.1002/2017JB014501

Colli, L., Bunge, H.-P., & Schuberth, B. S. A. (2015). On retrodictions of global mantle flow with assimilated surface velocities. *Geophysical Research Letters, 42*(20), 8341-8348. doi:10.1002/2015GL066001

Colli, L., Bunge, H. P., & Oeser, J. (2020). Impact of model inconsistencies on reconstructions of past mantle flow obtained using the adjoint method. *Geophysical Journal International, 221*(1), 617-639. doi:10.1093/gji/ggaa023

Conrad, C. P., Bianco, T. A., Smith, E. I., & Wessel, P. (2011). Patterns of intraplate volcanism controlled by asthenospheric shear. *Nature Geoscience, 4*, 317–321. doi:10.1038/ngeo1111 https://www.nature.com/articles/ngeo1111#supplementary-information

Cullen, A. B. (2010). Transverse segmentation of the Baram-Balabac Basin, NW Borneo: refining the model of Borneo's tectonic evolution. *Petroleum Geoscience, 16*(1), 3-29. doi:10.1144/1354-079309-828

Cullen, A. B. (2014). Nature and significance of the West Baram and Tinjar Lines, NW Borneo. *Marine and Petroleum Geology, 51*, 197-209. doi:https://doi.org/10.1016/j.marpetgeo.2013.11.010

Cullen, A. B., Zechmeister, M. S., Elmore, R. D., & Pannalal, S. J. (2012). Paleomagnetism of the Crocker Formation, northwest Borneo: Implications for late Cenozoic tectonics. *Geosphere, 8*(5), 1146-1169. doi:10.1130/GES00750.1

915 Deschamps, A., & Lallemand, S. (2002). The West Philippine Basin: An Eocene to early Oligocene
916 back arc basin opened between two opposed subduction zones. *Journal of Geophysical*
917 *Research: Solid Earth, 107*(B12), 2322. doi:10.1029/2001JB001706

918 Doust, H., & Sumner, H. S. (2007). Petroleum systems in rift basins - a collective approach in
919 Southeast Asian basins. *Petroleum Geoscience, 13*(2), 127-144. doi:10.1144/1354-079307-746

920 Fan, J., Zhao, D., Dong, D., & Zhang, G. (2017). P-wave tomography of subduction zones around
921 the central Philippines and its geodynamic implications. *Journal of Asian Earth Sciences, 146*, 76-
922 89. doi:https://doi.org/10.1016/j.jseaes.2017.05.015

923 Flament, N., Gurnis, M., & Müller, R. D. (2013). A review of observations and models of dynamic
924 topography. *Lithosphere, 5*(2), 189-210. doi:10.1130/L245.1

925 Fukao, Y., & Obayashi, M. (2013). Subducted slabs stagnant above, penetrating through, and
926 trapped below the 660 km discontinuity. *Journal of Geophysical Research: Solid Earth, 118*(11),
927 5920-5938. doi:10.1002/2013jb010466

928 Fuller, M., Ali, J. R., Moss, S. J., Frost, G. M., Richter, B., & Mahfi, A. (1999). Paleomagnetism of
929 Borneo. *Journal of Asian Earth Sciences, 17*(1), 3-24. doi:https://doi.org/10.1016/S0743-
930 9547(98)00057-9

931 Gurnis, M., Turner, M., Zahirovic, S., DiCaprio, L., Spasojevic, S., Müller, R. D., . . . Bower, D. J.
932 (2012). Plate tectonic reconstructions with continuously closing plates. *Computers &*
933 *Geosciences, 38*(1), 35-42. doi:https://doi.org/10.1016/j.cageo.2011.04.014

Hager, B. H., Clayton, R. W., Richards, M. A., Comer, R. P., & Dziewonski, A. M. (1985). Lower mantle heterogeneity, dynamic topography and the geoid. *Nature, 313*(6003), 541-545. doi:10.1038/313541a0

Hall, R. (1996). Reconstructing Cenozoic SE Asia. *Geological Society, London, Special Publications, 106*(1), 153-184. doi:https://doi.org/10.1144/GSL.SP.1996.106.01.11

Hall, R. (2002). Cenozoic geological and plate tectonic evolution of SE Asia and the SW Pacific: computer-based reconstructions, model and animations. *Journal of Asian Earth Sciences, 20*(4), 353-431. doi:https://doi.org/10.1016/S1367-9120(01)00069-4

Hall, R. (2012). Late Jurassic–Cenozoic reconstructions of the Indonesian region and the Indian Ocean. *Tectonophysics, 570-571*, 1-41. doi:https://doi.org/10.1016/j.tecto.2012.04.021

Hall, R., & Spakman, W. (2015). Mantle structure and tectonic history of SE Asia. *Tectonophysics, 658*, 14-45. doi:https://doi.org/10.1016/j.tecto.2015.07.003

Haq, B. U., & Al-Qahtani, A. M. (2005). Phanerozoic Cycles of Sea-Level Change on the Arabian Platform. *GeoArabia, 10*(2), 127-160.

Holloway, N. H. (1982). North Palawan Block, Philippines--Its Relation to Asian Mainland and Role in Evolution of South China Sea. *AAPG Bulletin, 66(9)*, 1355-1383. doi:10.1306/03B5A7A5-16D1-11D7-8645000102C1865D

Hosseini, K., Matthews, K. J., Sigloch, K., Shephard, G. E., Domeier, M., & Tsekhmistrenko, M. (2018). SubMachine: Web-Based Tools for Exploring Seismic Tomography and Other Models of

953 Earth's Deep Interior. *Geochemistry, Geophysics, Geosystems, 19*(5), 1464-1483.
954 doi:10.1029/2018GC007431

955 Hutchison, C. S. (2004). Marginal basin evolution: the southern South China Sea. *Marine and*
956 *Petroleum Geology, 21*(9), 1129-1148. doi:https://doi.org/10.1016/j.marpetgeo.2004.07.002

957 Jarvis, G. T., & McKenzie, D. P. (1980a). Convection in a compressible fluid with infinite Prandtl
958 number. *Journal of Fluid Mechanics, 96*(3), 515-583. doi:10.1017/S002211208000225X

959 Jarvis, G. T., & McKenzie, D. P. (1980b). Sedimentary basin formation with finite extension rates.
960 *Earth and Planetary Science Letters, 48*(1), 42-52. doi:https://doi.org/10.1016/0012-
961 821X(80)90168-5

962 Jian, Z., Jin, H., Kaminski, M. A., Ferreira, F., Li, B., & Yu, P.-S. (2019). Discovery of the marine
963 Eocene in the northern South China Sea. *National Science Review, 6*(5), 881-885.
964 doi:10.1093/nsr/nwz084

965 Karato, S.-I. (1993). Importance of anelasticity in the interpretation of seismic tomography.
966 *Geophysical Research Letters, 20(15)*, 1623–1626.

967 Kimura, J.-I., Sakuyama, T., Miyazaki, T., Vaglarov, B. S., Fukao, Y., & Stern, R. J. (2018). Plume-
968 stagnant slab-lithosphere interactions: Origin of the late Cenozoic intra-plate basalts on the East
969 Eurasia margin. *Lithos, 300-301*, 227-249. doi:https://doi.org/10.1016/j.lithos.2017.12.003

970 Lebedev, S., & Nolet, G. (2003). Upper mantle beneath Southeast Asia from S velocity
971 tomography. *Journal of Geophysical Research: Solid Earth, 108*(B1), 2048.
972 doi:10.1029/2000JB000073

973 Lei, J., & Zhao, D. (2006). Global P-wave tomography: On the effect of various mantle and core
974 phases. *Physics of the Earth and Planetary Interiors, 154*(1), 44-69.
975 doi:https://doi.org/10.1016/j.pepi.2005.09.001

976 Lei, J., Zhao, D., Steinberger, B., Wu, B., Shen, F., & Li, Z. (2009). New seismic constraints on the
977 upper mantle structure of the Hainan plume. *Physics of the Earth and Planetary Interiors,*
978 *173*(1), 33-50. doi:https://doi.org/10.1016/j.pepi.2008.10.013

979 Li, C., van der Hilst, R. D., Engdahl, E. R., & Burdick, S. (2008). A new global model forPwave
980 speed variations in Earth's mantle. *Geochemistry, Geophysics, Geosystems, 9*(5), Q0501.
981 doi:10.1029/2007gc001806

982 Liu, E., Wang, H., Tonguç Uysal, I., Zhao, J.-x., Wang, X.-C., Feng, Y., & Pan, S. (2017). Paleogene
983 igneous intrusion and its effect on thermal maturity of organic-rich mudstones in the Beibuwan
984 Basin, South China Sea. *Marine and Petroleum Geology, 86*, 733-750.
985 doi:https://doi.org/10.1016/j.marpetgeo.2017.06.026

986 Ma, P., Liu, S., Gurnis, M., & Zhang, B. (2019). Slab Horizontal Subduction and Slab Tearing
987 Beneath East Asia. *Geophysical Research Letters, 46*(10), 5161-5169.
988 doi:10.1029/2018GL081703

Matthews, K. J., Maloney, K. T., Zahirovic, S., Williams, S. E., Seton, M., & Müller, R. D. (2016). Global plate boundary evolution and kinematics since the late Paleozoic. *Global and Planetary Change, 146*, 226-250. doi:https://doi.org/10.1016/j.gloplacha.2016.10.002

Müller, R. D., Zahirovic, S., Williams, S. E., Cannon, J., Seton, M., Bower, D. J., . . . Gurnis, M. (2019). A global plate model including lithospheric deformation along major rifts and orogens since the Triassic. *Tectonics, 38*, 1884– 1907. doi:10.1029/2018TC005462

Nerlich, R., Colli, L., Ghelichkhan, S., Schuberth, B., & Bunge, H.-P. (2016). Constraining central Neo-Tethys Ocean reconstructions with mantle convection models. *Geophysical Research Letters, 43*(18), 9595-9603. doi:10.1002/2016GL070524

Pownall, J. M., Lister, G. S., & Spakman, W. (2017). Reconstructing subducted oceanic lithosphere by “reverse-engineering” slab geometries: The northern Philippine Sea Plate. *Tectonics, 36*(9), 1814-1834. doi:10.1002/2017TC004686

Pubellier, M., & Morley, C. K. (2014). The basins of Sundaland (SE Asia): Evolution and boundary conditions. *Marine and Petroleum Geology, 58*, 555-578. doi:https://doi.org/10.1016/j.marpetgeo.2013.11.019

Rangin, C., Spakman, W., Pubellier, M., & Bijwaard, H. (1999). Tomographic and geological constraints on subduction along the eastern Sundaland continental margin (South-East Asia). *Bulletin de la Société Géologique de France, 170*(6), 775-788. Retrieved from https://doi.org/

1007 Replumaz, A., & Tapponnier, P. (2003). Reconstruction of the deformed collision zone Between
1008 India and Asia by backward motion of lithospheric blocks. *Journal of Geophysical Research: Solid*
1009 *Earth, 108*(B6), 2285. doi:10.1029/2001JB000661

1010 Ritsema, J., Deuss, A., van Heijst, H. J., & Woodhouse, J. H. (2011). S40RTS: a degree-40 shear-
1011 velocity model for the mantle from new Rayleigh wave dispersion, teleseismic traveltime and
1012 normal-mode splitting function measurements. *Geophysical Journal International, 184*(3), 1223-
1013 1236. doi:10.1111/j.1365-246X.2010.04884.x

1014 Roberts, G. G., White, N., Hoggard, M. J., Ball, P. W., & Meenan, C. (2018). A Neogene history of
1015 mantle convective support beneath Borneo. *Earth and Planetary Science Letters, 496*, 142-158.
1016 doi:https://doi.org/10.1016/j.epsl.2018.05.043

1017 Sarr, A. C., Husson, L., Sepulchre, P., Pastier, A. M., Pedoja, K., Elliot, M., . . . Susilohadi. (2019).
1018 Subsiding Sundaland. *Geology, 47*(2), 119-122. doi:10.1130/G45629.1

1019 Schuberth, B. S. A., Bunge, H. P., Steinle-Neumann, G., Moder, C., & Oeser, J. (2009). Thermal
1020 versus elastic heterogeneity in high-resolution mantle circulation models with pyrolite
1021 composition: High plume excess temperatures in the lowermost mantle. *Geochemistry,*
1022 *Geophysics, Geosystems, 10*(1), Q01W01. doi:10.1029/2008GC002235

1023 Seno, T., & Maruyama, S. (1984). Paleogeographic reconstruction and origin of the Philippine
1024 Sea. *Tectonophysics, 102*(1), 53-84. doi:https://doi.org/10.1016/0040-1951(84)90008-8

1025 Shephard, G. E., Bunge, H. P., Schuberth, B. S. A., Müller, R. D., Talsma, A. S., Moder, C., &
1026 Landgrebe, T. C. W. (2012). Testing absolute plate reference frames and the implications for the

generation of geodynamic mantle heterogeneity structure. *Earth and Planetary Science Letters, 317-318*, 204-217. doi:https://doi.org/10.1016/j.epsl.2011.11.027

Shephard, G. E., Matthews, K. J., Hosseini, K., & Domeier, M. (2017). On the consistency of seismically imaged lower mantle slabs. *Scientific Reports, 7*(1), 10976. doi:10.1038/s41598-017-11039-w

Simmons, N. A., Myers, S. C., Johannesson, G., Matzel, E., & Grand, S. P. (2015). Evidence for long-lived subduction of an ancient tectonic plate beneath the southern Indian Ocean. *Geophysical Research Letters, 42*(21), 9270-9278. doi:10.1002/2015GL066237

Simmons, N. A., Schuberth, B. S. A., Myers, S. C., & Knapp, D. R. (2019). Resolution and Covariance of the LLNL-G3D-JPS Global Seismic Tomography Model: Applications to Travel time Uncertainty and Tomographic Filtering of Geodynamic Models. *Geophysical Journal International, 217*(3), 1543-1557. doi:10.1093/gji/ggz102

Steinberger, B. (2007). Effects of latent heat release at phase boundaries on flow in the Earth's mantle, phase boundary topography and dynamic topography at the Earth's surface. *Physics of the Earth and Planetary Interiors, 164*(1), 2-20. doi:https://doi.org/10.1016/j.pepi.2007.04.021

Stixrude, L., & Lithgow-Bertelloni, C. (2011). Thermodynamics of mantle minerals – II. Phase equilibria. *Geophysical Journal International, 184*(3), 1180-1213. doi:10.1111/j.1365-246X.2010.04890.x

Sun, Z., Lin, J., Qiu, N., Jian, Z., Wang, P., Pang, X., . . . Zhu, B. (2019). The role of magmatism in thinning and breakup of the South China Sea continental margin. *National Science Review, 6*(5), 871-876. doi:10.1093/nsr/nwz116

Tang, Q., & Zheng, C. (2013). Crust and upper mantle structure and its tectonic implications in the South China Sea and adjacent regions. *Journal of Asian Earth Sciences, 62*, 510-525. doi:https://doi.org/10.1016/j.jseaes.2012.10.037

Tapponnier, P., Peltzer, G., Le Dain, A. Y., Armijo, R., & Cobbold, P. (1982). Propagating extrusion tectonics in Asia: New insights from simple experiments with plasticine. *Geology, 10*(12), 611-616. doi:10.1130/0091-7613(1982)10<611:PETIAN>2.0.CO;2

Taylor, B., & Hayes, D. E. (1983). Origin and History of the South China Sea Basin. In D. E. Hayes (Ed.), *The Tectonic and Geologic Evolution of Southeast Asian Seas and Islands: Part 2* (Vol. 27, pp. 23-56): American Geophysical Union.

Wang, P., Huang, C.-Y., Lin, J., Jian, Z., Sun, Z., & Zhao, M. (2019). The South China Sea is not a mini-Atlantic: plate-edge rifting vs intra-plate rifting. *National Science Review, 6*(5), 902-913. doi:10.1093/nsr/nwz135

Wang, X.-C., Li, Z.-X., Li, X.-H., Li, J., Xu, Y.-G., & Li, X.-H. (2013). Identification of an ancient mantle reservoir and young recycled materials in the source region of a young mantle plume: Implications for potential linkages between plume and plate tectonics. *Earth and Planetary Science Letters, 377-378*, 248-259. doi:https://doi.org/10.1016/j.epsl.2013.07.003

1064 Wu, J., & Suppe, J. (2018). Proto-South China Sea Plate Tectonics Using Subducted Slab
1065 Constraints from Tomography. *Journal of Earth Science, 29*(6), 1304-1318. doi:10.1007/s12583-
1066 017-0813-x

1067 Wu, J., Suppe, J., Lu, R., & Kanda, R. (2016). Philippine Sea and East Asian plate tectonics since
1068 52 Ma constrained by new subducted slab reconstruction methods. *Journal of Geophysical*
1069 *Research: Solid Earth, 121*(6), 4670-4741. doi:doi:10.1002/2016JB012923

1070 Yang, T., Gurnis, M., & Zahirovic, S. (2016). Mantle-induced subsidence and compression in SE
1071 Asia since the early Miocene. *Geophysical Research Letters, 43*(5), 1901-1909.
1072 doi:10.1002/2016GL068050

1073 Yu, Y., Gao, S. S., Liu, K. H., Yang, T., Xue, M., Le, K. P., & Gao, J. (2018). Characteristics of the
1074 Mantle Flow System Beneath the Indochina Peninsula Revealed by Teleseismic Shear Wave
1075 Splitting Analysis. *Geochemistry, Geophysics, Geosystems, 19*(5), 1519-1532.
1076 doi:10.1029/2018GC007474

1077 Zahirovic, S., Matthews, K. J., Flament, N., Müller, R. D., Hill, K. C., Seton, M., & Gurnis, M.
1078 (2016). Tectonic evolution and deep mantle structure of the eastern Tethys since the latest
1079 Jurassic. *Earth-Science Reviews, 162*, 293-337. doi:10.1016/j.earscirev.2016.09.005

1080 Zahirovic, S., Müller, R. D., Seton, M., Flament, N., Gurnis, M., & Whittaker, J. (2012). Insights on
1081 the kinematics of the India-Eurasia collision from global geodynamic models. *Geochemistry,*
1082 *Geophysics, Geosystems, 13*(4), Q04W11. doi:10.1029/2011gc003883

Zahirovic, S., Seton, M., & D. Müller, R. (2014). The Cretaceous and Cenozoic tectonic evolution of Southeast Asia. *Solid Earth, 5*(1), 227-273. doi:10.5194/se-5-227-2014

Zhang, G., Shao, L., Qiao, P., Cao, L., Pang, X., Zhao, Z., . . . Cui, Y. (2019). Cretaceous–Palaeogene sedimentary evolution of the South China Sea region: A preliminary synthesis. *Geological Journal*, 1-22. doi:10.1002/gj.3533

Zhang, L.-S., & Scharer, U. (1999). Age and origin of magmatism along the Cenozoic Red River shear belt, China. *Contributions to Mineralogy and Petrology, 134*(1), 67-85. doi:https://doi.org/10.1007/s004100050469

Zhang, N., & Li, Z.-X. (2018). Formation of mantle "lone plumes" in the global downwelling zone — A multiscale modelling of subduction-controlled plume generation beneath the South China Sea. *Tectonophysics, 723*, 1-13. doi:https://doi.org/10.1016/j.tecto.2017.11.038

Zhao, M., Sibuet, J.-C., & Wu, J. (2019). Intermingled fates of the South China Sea and Philippine Sea plate. *National Science Review, 6*(5), 886–890. doi:10.1093/nsr/nwz107

Zhou, H., Xiao, L., Dong, Y., Wang, C., Wang, F., & Ni, P. (2009). Geochemical and geochronological study of the Sanshui basin bimodal volcanic rock suite, China: Implications for basin dynamics in southeastern China. *Journal of Asian Earth Sciences, 34*(2), 178-189. doi:https://doi.org/10.1016/j.jseaes.2008.05.001